Published in final edited form as:

Nat Immunol. 2023 August ; 24(8): 1265–1280. doi:10.1038/s41590-023-01545-7.

TRANSITIONAL DENDRITIC CELLS ARE DISTINCT FROM CONVENTIONAL DC2 PRECURSORS AND MEDIATE PRO-INFLAMMATORY ANTIVIRAL RESPONSES

Fernando Bandeira Sulczewski[1,5], **Raul A. Maqueda-Alfaro**[1,5], **Marcela Alcántara-Hernández**[1,5], **Oriana A. Perez**[2], **Sanjana Saravanan**[1], **Tae Jin Yun**[2], **David Seong**[1], **Rebeca Arroyo Hornero**[1], **Hayley M. Raquer-McKay**[1], **Eduardo Esteva**[2], **Zachary R. Lanzar**[1], **Rebecca A. Leylek**[1], **Nicholas M. Adams**[2], **Annesa Das**[2], **Adeeb H. Rahman**[3], **Andres Gottfried-Blackmore**[1,4], **Boris Reizis**[2,6], **Juliana Idoyaga**[1,6]

[1]Dept. of Microbiology & Immunology, and Immunology Program, Stanford University School of Medicine, Stanford, CA, 94305, USA

[2]Dept. of Pathology, New York University Grossman School of Medicine, New York, NY, 10016, USA

[3]Precision Immunology Institute, Department of Genetics and Genomic Science, Tisch Cancer Institute, and Human Monitoring Center, Icahn School of Medicine at Mount Sinai, New York, NY, 10029, USA.

[4]Division of Gastroenterology and Hepatology, Department of Medicine, Stanford University School of Medicine, Redwood City, CA, 94063, USA.

[5]These authors contributed equally

Abstract

High-dimensional approaches revealed emerging heterogeneity within dendritic cells (DC), including a population of transitional DC (tDC) present in mouse and human. However, tDC origin and relationship to other DC subsets are not fully understood. Here, we show that tDC are distinct from other well-characterized DC and conventional DC precursors (pre-cDC). We demonstrate that tDC originate from bone marrow progenitors shared with plasmacytoid DC (pDC). In the periphery, tDC contribute to the pool of $ESAM^{+}$ type 2 DC (DC2), and these DC2 harbor pDC-related developmental features. Different from pre-cDC, tDC have lower turnover, capture antigen, respond to stimuli, and activate antigen-specific naïve T cells, all characteristics of differentiated DC. Different from pDC, viral sensing by tDC results in IL-1β secretion and fatal

[6]Corresponding authors: jidoyaga@stanford.edu, Boris.Reizis@nyulangone.org.

AUTHOR CONTRIBUTIONS

F.B.S., R.M-A. and M.A-H. contributed equally to this by designing experiments, performing research, analyzing and interpreting the data, and writing the manuscript. The specific contributions of the authors are as follows: Conceptualization, F.B.S., R.M-A., M.A-H., and J.I., Methodology, F.B.S., R.M-A., M.A-H., O.A.P., B.R., and J.I.; Formal analysis, F.B.S., R.M-A., M.A-H., S.S., D.S., R.A.H., H.M.R-M, and E.E.; Investigation, F.B.S., R.M-A., M.A-H., S.S., T.J.Y., R.A.H., Z.R.L., R.A.L., and A.H.R.; Resources, O.A.P., N.M.A., A.D.; Visualization, F.B.S., R.M-A., M.A-H, S.S., D.S., R.A.H., H.M.R-M., and A.G-B.; Writing, F.B.S., R.M-A., M.A-H, A.G-B., B.R., and J.I, Funding Acquisition, B.R. and J.I.; Supervision, J.I.; Project administration, J.I.

COMPETING INTERESTS

J.I. serves on the scientific advisory board of Immunitas Therapeutics. All the other authors declare no competing interests.

immune pathology in a murine coronavirus model. Our findings suggest that tDC are a distinct pDC-related subset with a DC2 differentiation potential and unique pro-inflammatory function during viral infections.

Keywords

Dendritic cells; transitional DC; tDC; ASDC; pre-cDC; ESAM$^+$ DC2; IL-1β; murine coronavirus; murine hepatitis virus; pDC-like cells

INTRODUCTION

Dendritic cells (DC) are key immune sentinels comprised of subsets that initiate a broad range of immune responses[1]. Traditional nomenclature groups DC into conventional DC (cDC), which includes DC1 and DC2, and plasmacytoid DC (pDC). DC1 and DC2 are specialized in T cell activation[1], whereas pDC secrete interferon type I (IFN-I) following exposure to nucleic acids[2]. This classification does not include emerging DC, such as transitional DC (tDC), also reported as AXL$^+$ DC, ASDC or pre-cDC[3-6]. This is because the origin and *in vivo* function of tDC remains unclear.

All DC differentiate from a CX3CR1-expressing hematopoietic progenitor localized in the bone marrow (BM) through a FLT3L-dependent pathway[7-9]. Despite this common origin, immediate precursors for each subset have been reported. cDC arise from CD115-expressing conventional DC progenitors (pro-cDC)[8,9], with DC1 and DC2 originating from SiglecH$^-$Ly6C$^-$ and SiglecH$^-$Ly6C$^+$ immediate precursors, respectively[10,11]. pDC originate from a CX3CR1$^+$Ly6D$^+$ pro-pDC progenitor[7]. The molecular mechanisms dictating each DC subset lineage specification have been described[12,13]. DC1 require expression of several transcription factors (TFs) including IRF8[12,13], whereas pDC are dependent on TCF4[2]. DC2 are defined by the co-expression of the non-specific markers CD11c^{hi}CD11b$^+$MHCII$^+$CD172a$^+$; however, several molecular mechanisms converge into cells expressing these markers[12,14]. One of these mechanisms depends on the TF IRF4 and Notch2 signaling, and results in ESAM$^+$ DC2[15-18]. Another mechanism requires the TF KLF4, and results in CX3CR1$^+$ DC2[16,17,19]. Mouse ESAM$^+$ and CX3CR1$^+$ DC2 subpopulations seem to parallel human CD5$^+$ DC2 and CD14$^+$CD163$^+$ DC3, respectively[16,20-22], although further work is required to align these populations between species.

tDC were identified by single-cell high-dimensional approaches in human blood[3,5,6], and shown to be conserved between species[4]. Since human tDC express AXL and SIGLEC6, they were initially called AXL/SIGLEC6 DC (ASDC) or AXL$^+$ DC[3,6]. However, these markers are not conserved in mice. Therefore, the term “transitional DC” was suggested to highlight their spectrum of transcriptomic, phenotypic and functional features that spans cells similar to pDC and DC2[3,4,6]. This spectrum of features allows to sub-divide tDC into CD11c^{lo} tDC (hereafter called tDC^{lo}) more similar to pDC, and CD11c^{hi} tDC (hereafter called tDC^{hi}) similar to DC2. Until now, most studies have inadvertently analyzed one of these tDC sub-populations, which acquired different names, e.g., non-canonical DC (mainly tDC^{hi} cells)[4,23] and pDC-like cells (mainly tDC^{lo} cells)[24,25]. Consequently, it is still

uncertain if tDC^{lo} and tDC^{hi} are related, and if their pDC and DC2 features can be attributed to different origins. Moreover, tDC identity has been further challenged as their capacity to convert into cDC is becoming clearer in mouse and human[5,6,26]. However, whether tDC correspond to previously identified cDC precursors (pre-cDC) or are a different cell population is unknown. Importantly, given the lack of models to deplete tDC, the function of these cells has not yet been assessed *in vivo*.

Murine coronavirus (M-CoV), also known as murine hepatitis virus, can be used as a model to assess DC subset function *in vivo*. Early M-CoV containment is dependent on pDC capacity to rapidly produce IFN-I[27,28]. pDC elimination results in mild pathology characterized by higher liver viral titers, without increasing mortality[27,28]. Although these studies are informative, previous pDC depletion models, i.e., anti-BST2 antibody (Ab) and *Tcf4* conditional knockout mice (TCF4^{cKO}), also eliminate tDC, confounding interpretations. Consequently, it is imperative to evaluate pDC and tDC function during M-CoV infection using depletion models that allow their distinction *in vivo*.

Here, we address tDC origin, heterogeneity, and function *in vivo*. We found that tDC possess a core transcriptome that is unique to them. We resolve the developmental relationship of tDC^{lo} and tDC^{hi}, and demonstrate that both populations are related to pDC. We show that tDC convert into DC2, as recently reported[26]. However, tDC differentiate into ESAM^{+} DC2 that retain pDC developmental features. Importantly, tDC are not pre-DC2, indicating they represent a distinct source of DC2, and are not conventional precursors as suggested. Finally, tDC specifically produce IL-1β, which promotes fatal immunopathology during M-CoV infection. Altogether, our data indicate that the pDC lineage should be expanded to include tDC, a DC population that has a distinct role during viral infection and contributes to the developmental heterogeneity of DC2 in mice and humans.

RESULTS

tDC are a distinct DC population related to pDC

We queried if tDC have a unique core transcriptomic signature different from other DC subsets by performing bulk-RNAseq analysis of purified cells (Extended Data Fig.1a). Despite expressing pDC- and DC2- associated genes (Extended Data Fig.1b), tDC segregate from other DC subsets by Principal Component Analysis (PCA), implying distinct gene expression (Fig.1a and Extended Data Fig.1c). Differentially expressed gene (DEG) analysis revealed a tDC-specific signature including the expression of *Vim, Ngfr, Rab3il1, Cd209e, Chil5, L1cam, Ccr2 and Cd200r1* (Fig.1b; Supplementary Table1). tDC also differentially expressed *Klf12* and *Bcl11b*, TFs shown to be active by ATACseq analysis[29].

We applied scRNAseq to uncover cell-to-cell heterogeneity within tDC. We increased tDC representation by enriching CD135^{+} splenocytes and sorting two populations that were equally mixed for sequencing (Fig.1c). A total of 2,110 single cell transcriptomes were generated and 9 clusters identified by Seurat. Cell identity was assigned unbiasedly using CIBERSORTx and the bulk-RNAseq data, which resulted in one tDC cluster (Extended Data Fig.1d-e). To resolve the expected transcriptional heterogeneity within tDC, we instead applied K-nearest-neighbor-based Network graph drawing Layout (KNetL),

a dimensionality reduction that improves resolution. KNetL returned 8 clusters (Fig.1d), whose identity was again assigned unbiasedly (Extended Data Fig.1f; Supplementary Table2). tDC were represented in clusters 3 and 4, expressing the core genes identified by bulk-RNAseq, e.g., *Vim, Cd200r1, Chil5, Lgals3, Ms4a6c* (Fig.1e; Supplementary Table3). Cluster 3 expressed pDC-associated genes, e.g., *Bst2, Cd300c, Ly6c2* and *Tcf4*. Cluster 4 expressed DC2-associated genes, e.g., *Irf4 and Zbtb46*. The expression of these pDC- and DC2- associated genes was also observed by pair-wise comparisons of bulk-RNAseq (Extended Data Fig.1b; Supplementary Table4). We concluded that cluster 3 and 4 corresponded to tDC^{lo} and tDC^{hi}, respectively. In sum, despite transcriptional heterogeneity within the population, tDC express a core transcriptional program that defines their identity.

tDC^{lo} and tDC^{hi} share developmental features with pDC, including expression of pre-T cell receptor alpha and re-arranged IgH segments, and are decreased in *Itgax-Cre*$^{+/-}$ *Tcf4*$^{fl/fl}$ mice ($TCF4^{cKO}$)[4]. To rule out a cell extrinsic role for TCF4 in tDC development, we generated WT/$TCF4^{cKO}$ competitive bone marrow chimeras (BMC), and analyzed each DC population (Fig.1f-g)[4]. Similar to pDC, tDC^{lo} and tDC^{hi} were mostly derived from TCF4-proficient BM, indicating that TCF4 is intrinsically required for both tDC sub-populations (Fig.1g, Extended Data Fig.2a-b). To further evaluate the developmental relationship of tDC^{lo}, tDC^{hi} and pDC, we used pDC-specific lineage tracing models. Mice expressing Cre under the human CD2 promoter (*hCD2-iCre*$^{+/-}$) were bred to Cre-inducible EYFP reporter mice (*Rosa26*$^{LSL\text{-}EYFP+/-}$) to generate $hCD2^{EYFP}$ mice that label pDC[30,31]. EYFP labeling was observed in 100% of pDC, and ~85% of tDC^{lo} and tDC^{hi} (Fig.1h). We also generated a new fate mapping model based on the specific expression of CD300c by pDC[32]. When mice with Cre knocked into the *Cd300c* locus (*Cd300c*$^{Cre+/+}$) were bred with *Rosa26*$^{LSL\text{-}TdTomato+/-}$ mice ($CD300c^{TdT}$), tDC^{lo} and tDC^{hi} showed ~75% of TdTomato labeling relative to pDC (Fig.1i, Extended Data Fig.2c). Notably, in both lineage tracing models there was virtually no labeling (<10%) of DC1, but detectable (~25%) labeling of DC2, a result that will be discussed later. Altogether, these experiments cement the developmental relationship between tDC^{lo}, tDC^{hi} and pDC, suggesting a common origin.

tDC originate from BM progenitors at steady state

Mouse and human activated pDC can give rise to tDC[29,33]. We queried if pDC could give rise to tDC at steady state. Spleen and BM pDC were adoptively transferred to non-irradiated congenic mice and their outcome was followed over time (Fig.2a and Extended Data Fig.2d). All recovered donor-derived cells were pDC, indicating a non-pDC origin for tDC at steady state. Accordingly, tDC^{lo} and tDC^{hi} numbers were not affected by the temporal depletion of pDC in *BDCA2-DTR*$^{+/-}$ mice (Fig.2b).

We next asked if tDC could originate from BM progenitors by culturing unfractionated BM cells with FLT3L for DC differentiation[34]. $B220^{+}BST2^{+}SiglecH^{+}$ cells, previously characterized as pDC, could be further divided into $Ly6D^{+}CX3CR1^{-}$ pDC and $Ly6D^{-}CX3CR1^{+}$ tDC (Fig.2c). Both of these populations labeled the highest when using $hCD2^{EYFP}$ and $CD300c^{TdT}$ lineage tracing models (Fig.2d). BM-derived tDC peaked at 6-days and their development was abolished when OP9 stromal cells expressing Delta-like 1 (DL1) were added to the cultures (Fig.2e), as described for pDC[35]. Similar to their splenic

counterparts, BM-derived tDC expressed TCF4 and intermediate levels of pDC and cDC markers (Fig.2f). BM-derived tDC did not segregate into tDC^{lo} and tDC^{hi}, suggesting that *in vivo* signals are missing in the culture.

We concluded that tDC originate from BM progenitors at steady state. Interestingly, we detected a small number of tDC in blood but almost none in the BM, suggesting that tDC quickly exit the BM after development (Extended Data Fig.2e-f).

tDC originate from BM pro-pDC at steady state

Our data so far suggest that tDC originate from BM progenitors shared with pDC. We tested this unbiasedly by inferring the trajectory of tDC development in CD135-enriched BM cells analyzed by scRNAseq (Fig.3a). Application of the splenic tDC signature score to the clusters identified by Seurat labeled most pDC- and cDC- primed cells, which was attributed to tDC transcriptional similarities with pDC and DC2. Thus, the splenic pDC signature score was applied instead, which colored clusters expressing *Siglech* and *Ly6d*, but not *Csf1r* encoding CD115 (Fig.3b-c). Analysis of cells with a pDC score >0.15 resulted in 6 clusters (Fig.3d). Cluster 0 represented pDC expressing *Iglc3 and Klk1*, whereas cluster 5 represented tDC expressing *Lgals3, Ms4a6c* and *Cx3cr1* (Extended Data Fig.3a). Both cluster 0 and cluster 5 expressed *H2* genes and had gene enrichment for immune pathways, whereas clusters 2-4 were enriched for cell cycle pathways, a characteristic of progenitors (Extended Data Fig.3b). We then applied Slingshot and Velocity analyses to identify putative developmental relationships between these clusters (Fig.3e-f). Both algorithms revealed cluster 2 branching to pDC (cluster 0) and tDC (cluster 5). Gene expression dynamics demonstrated upregulation of *Ccr9 and Klk1* in pDC, and *Ms4a6c, Cx3cr1 and Lgals3* in tDC (Fig.3g). Besides expressing *Siglech* and *Ly6d* (Fig.3c), cluster 2 also expressed *Itgax* encoding for CD11c (Extended Data Fig.3a), markers of pDC progenitors (pro-pDC)[7].

We aimed to unbiasedly establish a gating strategy to isolate pro-pDC and evaluate their capacity to give rise to tDC. We performed CyTOF of CD135-enriched BM cells, and identified 7 clusters by UMAP. Marker enrichment analyses (MEM) pinpointed cluster-specific identifiers (Fig.3h-i). Cluster 6 was recognized as pDC and probably some tDC that were not resolved by the clustering algorithm. Cluster 4 corresponded to immature pDC expressing low levels of pDC markers. Cluster 3 had SiglecH, Ly6D, CX3CR1 and CD11c, an expression pattern consistent with pro-pDC. Cluster 2 and 7 both expressed CD115 and CX3CR1 but not SiglecH, corresponding to conventional DC progenitors (pro-cDC). Also, the expression pattern of cluster 2 and 7 correlated with pro-DC2 ($Ly6C^{hi}$) and pro-DC1 ($Ly6C^{lo}$), respectively. Based on the MEM analysis, a gating strategy to purify pro-pDC (cluster 3), immature pDC (cluster 4) and pro-cDC (clusters 2 and 7) was designed (Fig.3j), which was corroborated by overlaying onto the UMAP, and evaluating EYFP expression when using $hCD2^{EYFP}$ mice (Fig.3k-l). Only pDC, immature pDC and pro-pDC, but not pro-cDC, had >80% EYFP expression. Similar expression patterns were observed in $CD300c^{TdT}$ mice (Extended Data Fig.3c).

We assessed the potential of these progenitors to give rise to tDC following their adoptive transfer (Fig.3m and Extended Data Fig.3d-e). Immature pDC gave rise to pDC, whereas pro-cDC produced almost exclusively cDC, confirming the identity of the clusters. Pro-pDC

gave rise to tDC and pDC. Analysis of recovered tDC revealed the presence of mainly tDC^{lo} at 2-days but the appearance of tDC^{hi} at 4-days post-transfer, suggesting a trajectory of conversion from tDC^{lo} to tDC^{hi} (Fig.3n). Notably, recovered tDC^{lo} and tDC^{hi} labeled 100% with EYFP when transferred from $hCD2^{EYFP}$ mice, corroborating their common origin (Fig.3o). Surprisingly, pro-pDC also gave rise to DC2 (defined as in Fig.1f), as well as a small number of DC2 lacking CD11b, a population that is analyzed below (Fig.5). Interestingly, DC2 derived from pro-pDC were labeled 100% with EYFP when using $hCD2^{EYFP}$ mice (Fig.3o). In contrast, DC2 derived from pro-cDC were $EYFP^{-}$, indicating that $hCD2^{EYFP}$ can trace the heterogenous origins of DC2.

Finally, we reconciled our new gating strategy with previously described approaches. BM $CD115^{+}$, $CD127^{+}$, and double negative (DN) progenitors were purified and adoptively transferred (Extended Data Fig.4). tDC arose from DN $SiglecH^{+}Ly6D^{+}$ progenitors. When these DN progenitors were overlaid onto our UMAP of CyTOF data, we observed they fell within clusters 3 and 4, suggesting this prior gating strategy does not separate pro-pDC from immature pDC (Fig.3p). Even though the majority of the $CD115^{+}Ly6C^{+/-}$ progenitors fell within pro-cDC in the UMAP, a small fraction overlapped with pro-pDC (Fig.3p). $CD127^{+}SiglecH^{+}Ly6D^{+}$ cells, suggested to be the immediate pDC progenitor[25], partially overlapped with cluster 4 but not cluster 3, indicating that this gate captures a few immature pDC but not pro-pDC. Altogether, our gating strategy provides improved resolution of BM progenitors.

We concluded that tDC originate from a $CD115^{-}$ BM progenitor that expresses SiglecH, Ly6D, CD11c and CX3CR1, and corresponds to the recently described pro-pDC progenitor[7].

Splenic tDC differentiate into $ESAM^{+}$ DC2

In $hCD2^{EYFP}$ and $CD300c^{TdT}$ lineage tracing models, ~25% of DC2 were labeled (Fig.1h-i). Thus, we queried if tDC could convert into these labeled DC2 (Fig.4a and Extended Data Fig.5a). tDC acquired DC2 markers, specifically $CD11c^{hi}MHCII^{+}CD172a^{+}$ expression, following adoptive transfer into non-irradiated congenic recipients. At 2-days post-transfer, some DC2 lacked CD11b expression ($CD11b^{-}$ DC2), but most were $CD11b^{+}$ by 4-8-days suggesting a transition from a $CD11b^{-}$ to a $CD11b^{+}$ DC2 (evaluated in Fig.5). When tDC were purified from $hCD2^{EYFP}$ mice, ~85% of recovered DC2 were $EYFP^{+}$ independently of their expression of CD11b (Fig.4b). This data suggests that tDC can convert into DC2.

We then aimed at evaluating if tDC conversion into DC2 occurs *in vivo* at homeostasis. Given that tDC express CX3CR1 and are labeled in $hCD2^{EYFP}$ mice, we hypothesized that they would be specifically depleted in *hCD2-iCre*$^{+/-}$ x *Cx3cr1*$^{LSL\text{-}DTR+/-}$ mice. One DT dose resulted in tDC depletion without affecting other DCs (Extended Data Fig.5b). Continuous DT administration for 7-days also depleted pDC due to elimination of pro-pDC, as described[7](Extended Data Fig.5b-c); however, total DC2 numbers were unaffected. To reconcile the adoptive transfer and tDC depletion experiments, we crossed $hCD2^{EYFP}$ with *Cx3cr1*$^{LSL\text{-}DTR+/-}$ mice ($hCD2^{EYFP}$ $CX3CR1^{DTR}$), which allowed us to monitor $EYFP^{+}$ DC2 following DT inoculation. tDC and pDC were decreased 7-days post-DT administration, but total DC2 numbers were unaffected (Fig.4c). However, the fraction of

EYFP$^+$ DC2 decreased ~2-fold, with a corresponding increase in EYFP$^-$ DC2 (Fig.4d). Thus, tDC are a source of a fraction of DC2 *in vivo*, which can be traced in hCD2^{EYFP} mice. To confirm that EYFP-labeling distinguishes tDC-derived DC2, we evaluated the expression of IgH rearrangements, a feature of tDC and pDC that is passed to progeny cells[4]. IgH rearrangements were detected in EYFP$^+$ but not EYFP$^-$ DC2 (Extended Data Fig.5d). Notably, CD11b$^-$ DC2 were also eliminated post-DT administration, supporting a relationship with tDC (Fig.4c).

To gain a comprehensive understanding of tDC-derived DC2, we sorted EYFP$^+$ and EYFP$^-$ DC2 from hCD2^{EYFP} mice and performed bulk-RNAseq (Fig.4e). DEG analysis revealed that EYFP$^-$ DC2 uniquely expressed *Fcgr2b* (encoding CD32), *Cx3cr1*, *Clec12a*, *Clec7a*, resembling CX3CR1$^+$ DC2[16,17](Supplementary Table5). Despite a small contamination with EYFP$^+$ lymphoid cells, tDC-derived EYFP$^+$ DC2 expressed higher levels of *Gpr4* and the Notch target *Dtx1*, genes expressed by ESAM$^+$ DC2[16,17]. Flow cytometry confirmed that EYFP$^+$ were contained within ESAM$^+$ DC2 and not CX3CR1$^+$ DC2 (Fig.4f). When comparing relative expression of DC2 markers between the different DC2 subpopulations, EYFP$^+$ ESAM$^+$ DC2 lacked expression of CD32, CLEC7A, CLEC12A, all markers of CX3CR1$^+$ DC2[16,17](Fig.4g). EYFP$^+$ ESAM$^+$ DC2 expressed CD4 and CD5, and differed from EYFP$^-$ ESAM$^+$ DC2 in their higher and lower levels of CD24 and CD11b, respectively (Fig.4g-h). These results were confirmed using CD300c^{TdT} mice (Extended Data Fig.5e). Thus, tDC can convert into a subpopulation of DC2 expressing ESAM.

Human tDC may give rise to DC1 and DC2[5]. However, our mouse data indicates that tDC only convert into ESAM$^+$ DC2, which is presumably the equivalent to human CD5$^+$ DC2[16]. We re-evaluated human tDC conversion into cDC using CyTOF and unbiased Scaffold analysis. Freshly isolated blood tDC localized in the tDC landmark node (day 0). By 2-days in culture, ~60% tDC mapped to DC2, but not DC1 (Fig.4i-j). We observed a few tDC localized in the pDC landmark node (~5%), which was attributed to a loss of AXL. Human tDC upregulated CD33, CD172a, CD32, CD1c, but not the DC1-specific marker CLEC9A (Fig.4k). tDC also upregulated CD5, but failed to upregulate CD14 and CD163, suggesting conversion into DC2, but not DC3[22]. Altogether, our data indicate that tDC differentiate into mouse ESAM$^+$ DC2 and human CD5$^+$ DC2.

tDC are distinct from cDC-committed precursors

We sought to clarify tDC relationship with previously described DC2-committed precursors. We focused on the spleen because of the high tDC numbers vs BM or blood. Splenic precursors have differential lineage commitment based on the expression of SiglecH and Ly6C[11]. SiglecH$^+$Ly6C$^+$ (pop#5; Fig.5a) are recognized as uncommitted precursors that give rise to DC1 and DC2, whereas SiglecH$^-$Ly6C$^-$ (pop#3; Fig.5a) and SiglecH$^-$Ly6C$^+$ (pop#4; Fig.5a) are DC1- and DC2-committed precursors, respectively. We observed that EYFP labeling was similar between pop#5 and tDC when using hCD2^{EYFP} mice (Fig.5b). Contrarily, only ~25% of pop#4 and ~10% of pop#3 were EYFP-labeled. We then mapped these 3 splenic precursor populations onto a UMAP of all splenic DC. Pop#5 mapped within tDC; however, only fell within tDC^{lo} and represented ~25% of all the tDC cluster (Fig.5c-d). Pop#3 mapped within pre-DC1, although some mapped within DC1 suggesting that the

reported gating strategy includes contaminating mature XCR1^{+} DC1. Most of pop#4 (~85%) mapped outside the tDC gate, with only ~4% contaminating all tDC. Thus, tDC are distinct from pop#3 and pop#4. Notably, our lineage tracing data implies that pop#5 are tDC and not uncommitted precursors that give rise to pop#3 and pop#4, as suggested[11].

We designed a gating strategy to analyze pop#3 and pop#4 precursors without contaminating DC1 or tDC (called pre-DC1 and pre-DC2, hereafter) (Fig.5e). Our new gating strategy yielded pre-DC2 and pre-DC1 with ~10% EYFP labeling in hCD2^{EYFP} mice (Fig.5f). It also allowed separation of CD11b^{-} DC2, that label similar to tDC in hCD2^{EYFP} mice. As expected, EYFP labeling was only evident in ESAM^{+} DC2, but not in CX3CR1^{+} DC2. We validated our new gating strategy by mapping all populations onto our UMAP of CyTOF data (Fig.5g). tDC^{lo}, tDC^{hi}, CD11b^{-} DC2 and pre-DC2 mapped in different locations of the UMAP, indicating distinct phenotype. tDC^{lo} and pre-DC2 shared the expression of CX3CR1, but tDC^{lo} expressed higher levels of Ly6C, IRF8, TCF4 and SiglecH (Fig.5g). tDC^{hi} expressed CD11c, CD172a, MHCII and some CD8, all markers absent in pre-DC2. We observed higher expression of CCR2 in pre-DC2, a chemokine receptor known to be expressed in cDC precursors[36]. Notably, CD11b^{-} DC2 and DC2 shared most markers; however, CD11b^{-} DC2 expressed CD135 and low levels of CD24. Interestingly, pDC, tDC and CD11b^{-} DC2 expressed higher levels of CD45RB and CD45RA, suggesting that these markers may be useful to identify these cells in models other than hCD2^{EYFP} mice. Thus, our multi-dimensional analyses unmasked key phenotypic differences between tDC and pre-DC2.

We compared tDC and pre-DC2 capacity to give rise to DC2 after their adoptive transfer (Fig.5h). Pre-DC1 were used as controls, and only gave rise to DC1. Transferred pre-DC2 only gave rise to DC2, whereas tDC^{lo}, tDC^{hi}, CD11b^{-} DC2 also gave rise to some tDC and CD11b^{-} DC2 (Fig.5h). Pre-DC2 gave rise to EYFP^{-} cells, whereas tDC^{lo}, tDC^{hi} and CD11b^{-} DC2 gave rise to EYFP^{+} cells when purified from hCD2^{EYFP} mice (Fig.5i). Importantly, all tDC-related populations gave rise to CX3CR1^{-} but not CX3CR1^{+} DC2, and most of these cells (~70%) expressed ESAM (Fig.5i). Transferred tDC^{lo} cells gave rise to ~60% tDC^{hi} by 4-days indicating a transition from tDC^{lo} to tDC^{hi} (Fig.5j). Similarly, few tDC were recovered when tDC^{hi} were transferred, and none when CD11b^{-} DC2 were transferred. Together, this transfer data implies a transition from tDC^{lo} → tDC^{hi} → CD11b^{-} DC2 → ESAM^{+} DC2.

To further contrast tDC and pre-DC2, we compared their turnover rate, which is high in DC precursors[37], by performing a BrdU “pulse-chase” experiment (Extended Data Fig.6a). Pre-DC2 had the highest turnover rate, clearing ~90% of BrdU by 8-days (Fig.5k), whereas tDC^{lo} and tDC^{hi} only cleared ~50% and ~35% of BrdU. Accordingly, Ki-67 proliferation marker was highest in pre-DC2 (Extended Data Fig.6b). Thus, tDC have a low turnover rate in comparison to pre-DC2, which could explain why we did not observe a DC2 decrease after tDC depletion for 7-days. Consistently, analysis of hCD2^{EYFP} CX3CR1^{DTR} mice following 10-days of DT treatment showed ~30% DC2 decrease (Fig.5l). Only ESAM^{+} EYFP^{+} DC2, but not CX3CR1^{+} DC2 were decreased (Fig.5l, Extended Data Fig.6d). Importantly, pre-DC2 were not affected, which may explain the maintenance of ~50%

ESAM$^+$ DC2 following tDC depletion. Similarly, monocytes, neutrophils and lymphocytes were not affected (Extended Data Figure 6e)

Altogether, our data show that tDC are distinct from pre-DC2 in their phenotype, turnover and proliferative rate. It also implies that ESAM$^+$ DC2 have two different origins, i.e., BM CD115$^-$ pro-pDC and CD115$^+$ pro-cDC.

tDC require IRF4 to convert into DC2

The TFs IRF4 and KLF4 are distinctly required for ESAM$^+$ and CX3CR1$^+$ DC2 development, respectively[12,17,19]. We queried if IRF4 is necessary for tDC conversion into ESAM$^+$ DC2. We correlated *Irf4* expression with EGFP levels following the *Itgax-Cre*-mediated recombination of *Irf4$^{fl/fl}$* (IRF4^{cKO} mice), and found highest EGFP expression in tDC^{hi} (Fig.6a). IRF4^{cKO} mice had slightly increased tDC and decreased DC2 numbers, specifically ESAM$^+$ DC2 (Fig.6b). Interestingly, IRF4^{cKO} mice had almost no CD11b$^-$ DC2, but normal numbers of pre-DC2, suggesting that only tDC^{hi} → CD11b$^-$ DC2 → ESAM$^+$ DC2, but not pre-DC2 ESAM$^+$ DC2 conversion was affected. We next generated competitive BMC to evaluate the intrinsic role of IRF4 in each population. tDC did not require IRF4; however, CD11b$^-$ DC2 were IRF4-dependent as these cells derived almost exclusively from IRF4-proficient BM (Fig.6c). Contrarily, IRF4 was not required for pre-DC2. As expected, ESAM$^+$ but not CX3CR1$^+$ DC2 required IRF4.

We validated our results by performing adoptive transfer experiments (Fig.6d). IRF4^{control} tDC yielded DC2, whereas IRF4^{cKO} tDC yielded no cells by 8-days (Fig.6d). IRF4^{cKO} tDC still yielded some tDC at 4-days post-transfer, suggesting arrested conversion to DC2. Similar results were observed when tDC from FLT3L BM cultures were purified and re-cultured *in vitro* (Extended Data Fig.6c). Altogether, our results indicate that tDC^{hi} → CD11b$^-$ DC2 → ESAM$^+$ DC2 conversion is dependent on IRF4.

tDC respond to TLR agonists and promote T cell proliferation

Mouse and human tDC are able to respond to the TLR9 agonist CpG, upregulate MHCII/costimulatory molecules, and promote the proliferation of allogenic T cells[4], suggesting that these cells are not just precursors, but harbor functions of differentiated DC. To look further at the functional capabilities of tDC vs cDC, we first evaluated TLR expression. tDC expressed TLR7 and TLR9, but low levels of TLR4 and TLR3 (Extended Data Fig.7a). tDC^{lo} and tDC^{hi} have lower basal expression of MHCII and CD86[4], but were able to quickly upregulate these markers post-TLR7 or TLR9 stimulation (Extended Data Fig.7b-c; see[4] for TLR9). Also, as shown for TLR9[4], tDC produced IL-12p40 in response to TLR7. Thus, tDC quickly respond to TLR7 and TLR9 agonists.

We assessed unbiasedly the transcriptional changes that tDC undergo following TLR stimulation. Splenocytes from hCD2^{EYFP} mice were stimulated with a TLR cocktail to activate all DC simultaneously (TLR3, 4, 7, and 9) and bulk-RNAseq was performed 3hr later in purified cells. tDC$^{lo\text{-}hi}$ were analyzed as one population, and DC2 were divided into EYFP$^+$ and EYFP$^-$ DC2. PCA showed that stimulated DC clustered separately from unstimulated cells, accounting for ~50% of variance (Fig.7a). Stimulated tDC clustered independently from other DC subsets, implying that their gene expression program was

shaped by their activation status and core signature genes, as previously shown for pDC and cDC[38]. Activated tDC upregulated pathways related with DC maturation, including hallmark inflammatory, TNF, interferon responses, and genes of the IL-1-family (*Il1b*, *Il1r1*, and *Il1rap*)(Fig.7b-c). Thus, tDC upregulate key programs for the induction of adaptive immune responses, a feature shared with pDC and cDC.

We next evaluated if tDC share other functions with cDC, e.g., antigen capture, processing and presentation to T cells. FITC-beads or PKH-labeled sheep red blood cells (SRBC) were administered i.v. for their *in vivo* capture by splenic DC subsets. FITC-beads and PKH-labeled SRBC were taken up comparably between tDC and cDC (Extended Data Fig.7d-e). Notably, pre-DC2 or pre-DC1 were unable to capture antigen *in vivo*. tDC also captured, processed, and presented ovalbumin (OVA) protein to naïve antigen-specific $CD4^+$ T cells, which underwent several rounds of division (Fig.7d). Although tDC^{hi} were more efficient than tDC^{lo} at activating T cell proliferation, both populations were significantly better than pDC. tDC^{hi} and $CD11b^-$ DC2 were slightly better than $ESAM^+$ DC2, which may be consequence of differential survival of these cells in culture, an observation that remains to be confirmed.

In summary, tDC respond to TLR7/9 stimulation, capture, process and present antigen to T cells, indicating that they are not just DC2 precursors but a functional DC population.

tDC promote immunopathology during coronavirus infection

Finally, we sought to understand tDC function *in vivo*. We hypothesized that tDC would play a role during viral infection, given their developmental relationship with pDC and expression of TLR7/9. We chose M-CoV since pDC are known to be essential for its early containment[27,28]. Similar to influenza infection[4], tDC accumulated in the primary infected tissue, which is the liver for M-CoV (Extended Data Fig.8a-c). We reasoned that models for the specific depletion of pDC and tDC ($hCD2^{EYFP}$ $CX3CR1^{DTR}$ + DT mice; $pDC^{\Delta}tDC^{\Delta}$ mice hereafter) vs pDC only (*BDCA2-DTR* + DT mice; pDC^{Δ} mice hereafter) would allow us to dissect tDC function during infection. $pDC^{\Delta}tDC^{\Delta}$ mice depleted liver pDC and tDC, whereas pDC^{Δ} mice depleted only pDC (Fig.8a). None of these models affected other liver immune cells (Extended Data Fig.8a-b, d).

Weight change in infected mice was used as a measure of infection severity. Control mice developed asymptomatic infection with almost no weight loss, whereas IFN-I receptor knockout mice ($IFNR1^{KO}$) displayed critical pathology and died by 2-days post-infection (p.i.), as described[27](Fig.8b). By 3-days p.i., pDC^{Δ} and $pDC^{\Delta}tDC^{\Delta}$ mice started to lose weight. By 5-days p.i., pDC^{Δ} mice were moribund experiencing severe pathology and >20% weight loss. In contrast, $pDC^{\Delta}tDC^{\Delta}$ mice displayed milder pathology and complete survival. Severe pathology in pDC^{Δ} mice correlated with exacerbated liver damage measured by increased serum alanine transaminase (ALT), pro-inflammatory monocyte and neutrophil infiltration (Fig.8c-d). pDC^{Δ} mice also had a late spike in viral titers (5-days p.i.), likely consequence of excessive liver damage (Fig.8e and Extended Data Fig.8f). On the other hand, milder pathology in $pDC^{\Delta}tDC^{\Delta}$ mice correlated with less liver damage and pro-inflammatory cells. To confirm that eliminating both pDC and tDC resulted in milder pathology to M-CoV, we also infected $TCF4^{cKO}$ mice, which harbor significantly less

numbers of liver pDC/tDC without affecting cDC (Extended Data Fig.9a). Similar to $pDC^{\Delta}tDC^{\Delta}$ mice, $TCF4^{cKO}$ mice had mild pathology, limited liver damage and modest increase in viral titers, as previous observed[28](Extended Data Fig.9b-d). These results suggest that severe M-CoV pathology is not mediated by the sole elimination of pDC, which occurs in both mouse models, but rather by tDC presence in pDC-depleted mice.

To investigate the underlying tDC-mediated mechanism driving severe pathology, we analyzed cytokines/chemokines in serum 2-days p.i. (Extended Data Fig.9e). Severe pathology in pDC^{Δ} mice correlated with a significant increase in pro-inflammatory cytokines and chemokines, including IL-1β, IL-18, TNF, IL-6, which was not observed in $pDC^{\Delta}tDC^{\Delta}$ mice. Acutely increased serum levels of IL-12p70 and IFNγ in pDC^{Δ} mice suggest augmented innate lymphocyte numbers or function. However, natural killer (NK) and innate lymphocyte 1 (ILC1) numbers were not affected, and their depletion did not ameliorate M-CoV infection severity in pDC^{Δ} mice, indicating that these cells do not mediate pathology (Extended Data Fig.8d and 9f-g). Among the other pro-inflammatory cytokines upregulated in pDC^{Δ} mice, IL-1β could mediate higher chemokine/cytokine levels resulting in increased liver damage[39,40]. Indeed, IL-1β increased 2-5-fold in the serum of pDC^{Δ} vs control and $pDC^{\Delta}tDC^{\Delta}$ mice, as early as 2-days p.i. (Fig.8f). A single dose of anti-IL-1β blocking antibody in pDC^{Δ} mice significantly reduced pathology, i.e., lower weight loss, ALT levels, liver-infiltrating leukocytes and viral titers (Fig.8g-j and Extended Data Fig.9h).

So far, our data suggest that tDC mediate severe pathology in pDC^{Δ} mice through a dysregulated IL-1β production, which is consistent with an increase in *Il1b* and related genes following TLR stimulation (Fig.7c). We tested tDC capacity to secrete IL-1β in response to M-CoV. Purified tDC secreted IL-1β at higher levels than either pDC, DC1, $EYFP^{+}$ and $EYFP^{-}$ DC2 (Fig.8k), whereas pDC secreted TNF, IL-6 and some IL-12p70 (Extended Data Fig.9i). We extended these observations to human tDC stimulated with CpG (Fig.8l-n). Again, human tDC rapidly produced IL-1β, which was more prominent than either pDC or cDC. Moreover, human tDC also produced IL-1β in response to influenza and cytomegalovirus (CMV)-infected lung fibroblasts (MRC5), whereas pDC produced IFN-α (Fig.8m-n, and[41]). Thus, tDC have a distinct capacity to rapidly produce IL-1β in response to viruses and their mimics, a feature that is conserved in mouse and human.

In summary, our data supports a model in which dysregulated secretion of IL-1β by tDC is associated with severe coronavirus pathology.

DISCUSSION

In this study, we unravel tDC identity, development and function. Our data show that tDC are not pre-DC2 as suggested, but rather a DC population that develops from BM pro-pDC. tDC have functions of cDC, and a distinct capacity to rapidly produce IL-1β in response to viruses, which promotes fulminant liver pathology during M-CoV infection. Finally, tDC distinctly convert into mouse $ESAM^{+}$ DC2 or human $CD5^{+}$ DC2. Our data indicate that current definitions of the DC compartment should be expanded to encompass tDC, a

pDC-related DC subset that has a distinct role during viral infections and contributes to the developmental heterogeneity of DC2 in mice and humans.

It has been suggested that tDC^{lo} and tDC^{hi} may have different developmental origins, i.e., lymphoid vs myeloid, respectively. Here, we show ample evidence that this is not the case. Both tDC^{lo} and tDC^{hi} share a core transcriptome that differentiate them from other subsets, as also observed by the group of M. Dalod[24]. These subpopulations exhibit developmental features shared with pDC, such as IgH rearrangements and PTCRA expression[4], and the need of TCF4 for their differentiation. Both tDC^{lo} and tDC^{hi} labeled similarly to pDC when using two different tracing mouse models (hCD2^{EYFP} and CD300c^{TdT}), and emerged from pro-pDC at steady state. Further experiments are needed to evaluate if pro-pDC are bi-potent progenitors giving rise to tDC and pDC. Finally, tDC^{lo} gives rise to tDC^{hi} after adoptive transfer experiments. Thus, tDC^{lo} and tDC^{hi} are different states within the same population of cells. As tDC^{lo} transition to tDC^{hi}, they upregulate several DC2 TFs including ZBTB46[4]. Thus, ZBTB46 expression is one of the many transitional features of this population and should not be interpreted as an origin marker from a pro-cDC progenitor[25]. In fact, ZBTB46 regulates cDC activation rather than development[42].

Adoptive transfer experiments revealed that tDC convert exclusively into ESAM^{+} DC2, passing through a CD11b^{-} DC2 stage. Two fate tracing models suggest that 30-40% of ESAM^{+} DC2 are tDC-derived. This was confirmed by the presence of IgH rearrangements. Finally, tDC-derived ESAM^{+} DC2, but not CX3CR1^{+} DC2, are depleted by the administration of DT into hCD2^{EYFP} CX3CR1^{DTR}. During the preparation of this manuscript, a report by Rodriguez *et al.*[26] implied that pDC-like cells, which encompass a portion of tDC^{lo}, convert into CX3CR1^{+} DC2 following adoptive transfer into irradiated recipient mice. The discrepancies between our observations and Rodriguez *et al.* may arise from different gating strategies to define DC2, as well as the cell transfer conditions. Rodriguez *et al.* used only two markers to define DC2, MHCII^{+} and CD172a^{+}. However, this strategy likely results in contamination of DC2 with ESAM^{-}CX3CR1^{+} tDC^{hi}. Further, different from Rodriguez *et al.*, our cell transfer experiments were performed in non-irradiated congenic recipients to avoid unphysiological proliferation of DC following radiation. Finally, our data unraveling tDC conversion into mouse ESAM^{+} DC2 parallels human tDC conversion into CD5^{+} DC2, but not CD14^{+} DC3. Notably, human DC3 are known to develop via a GM-CSF-dependent monocyte/dendritic cell progenitor (MDP)[20,21]. Although the origin of mouse DC3 requires further investigation, we show here that tDC arise from the FLT3L-dependent pro-pDC pathway, and not MDP.

We show that tDC are distinct from pre-DC2. tDC trace back to pro-pDC and, consequently, share developmental features with pDC. These features are only observed in tDC and tDC-derived DC2, but not pre-DC2 derived DC2. Second, tDC have phenotypic differences with pre-DC2 . Despite that tDC and pre-DC2 give rise to ESAM^{+} DC2, tDC do so passing through a CD11b^{-} DC2 stage. Different from pre-DC2, tDC have lower turnover and proliferation rate. Unlike pre-DC2, very few tDC reside in the BM suggesting that these cells exit the organ quickly post-development. Finally, mouse tDC exhibit functions of cDC including widespread transcriptional changes following TLR stimulation, antigen capture, and activation of antigen-specific T cells; functions conserved between species[4-6].

Importantly, tDC require different TF than pre-DC2. TCF4 is required for tDC development from pro-pDC, whereas IRF4 is required for tDC^{hi} → CD11b^{-} DC2 → ESAM^{+} DC2 conversion; however, IRF4 does not seem to be necessary for pre-DC2 → ESAM^{+} DC2 conversion. Notably, IRF4^{cKO} mice have reduced CD24^{+} DC2 in several tissues[13,15], consistent with our observation that CD24 expression is slightly higher in splenic tDC-derived ESAM^{+} DC2. Further studies are needed to evaluate the contribution of tDC and pre-DC2 to the DC2 compartment in different tissues. Nevertheless, the unique characteristics of tDC warrant their distinction from pre-DC2.

Interestingly, in situations where tDC development is impaired at the level of pro-pDC (e.g., TCF4^{cKO} mice), DC2 are present at normal numbers suggesting that they are maintained by pre-DC2. Similarly, in situations where pre-DC2 development is impaired (e.g., *Clec9a*^{Cre} *Rosa26*^{DTA} mice), DC2 are present at normal numbers but harbor IgH rearrangements[43], suggesting they may be derived from tDC. Thus, the ESAM^{+} DC2 compartment seems to be maintained by two distinct developmental pathways that converge into cells that are phenotypically similar (Extended Data Fig.10). The contribution of these two distinct developmental pathways to the DC2 pool may be signaled by environmental cues (e.g., age and IFN-I availability)[44,45]. To dissect the *in vivo* functions of these two developmental pathways, it would be helpful if DC2 origin is reflected in their name, e.g., tDC2 for tDC-derived DC2 and cDC2 for pre-DC2-derived DC2. Importantly, it is imperative to identify surface markers to distinguish these two developmental origins of DC2, and CD45RA and CD45RB described here may assist this goal.

Mouse and human tDC distinctively produce high levels of IL-1β in response to viruses, which likely plays a protective role during immune responses. However, the dysregulated IL-1β secretion by tDC culminated in excessive immunopathology during M-CoV infection. This excessive immunopathology recapitulates several features of SARS-CoV-2 including higher viral titers, neutrophil and monocyte recruitment, and excessive tissue damage[46,47]. Notably, similar to our mouse depletion model, pDC from severe SARS-CoV-2 patients are dysfunctional and unable to produce IFN-I[48,49], suggesting that the dysregulated tDC-mediated IL-1β pathway described here may be active also in humans. Accordingly, anti-IL-1β Abs and IL-1β/α inhibitors have shown benefit in SARS-CoV-2 patients[50]. Altogether, our work unveils an innate immune balance between efficient antiviral vs pro-inflammatory response that is controlled by developmentally related cells, pDC and tDC, suggesting that these two DC populations form a distinct lineage of cells with key complementary functions during viral infections.

METHODS

Human specimens and PBMCs

Donors provided informed consent in accordance with IRB protocols approved by the Stanford University Administrative Panel on Human Subjects in Medical Research. De-identified blood and buffy coats were obtained from healthy adult human donors (20-45 years old) following the guidelines of the Research and Laboratory Environmental Health and Safety program of Stanford University or from the New York Blood Center

(NYBC). Peripheral blood mononuclear cells (PBMCs) were isolated by density gradient centrifugation using Ficoll-Paque PLUS (GE Healthcare).

Mice

Mice (reporting summary) were purchased from The Jackson Laboratory or Charles River. *Cx3cr1*$^{EGFP+/-}$ were crossed with CD45.1 mice in-house. *Itgax-Cre*$^{+/-}$ mice were crossed to *Irf4*$^{fl/fl}$ in-house and screened routinely for the appearance of *Irf4* germline deletions[51]. Side by side comparison showed that *Itgax-Cre*$^{+/-}$ x *Irf4*$^{fl/fl}$ and *Itgax-Cre*$^{+/-}$ x *Irf4*$^{fl/deletion}$ mice have similar phenotypes, so mice were pooled for experiments and labeled as IRF4^{cKO}. IRF4^{control} group includes *Itgax-Cre*$^{-/-}$ x *Irf4*$^{fl/fl}$ and *Itgax-Cre*$^{-/-}$ x *Irf4*$^{fl/deletion}$ mice. The *Cd300c*^{Cre} strain was generated by knocking Cre recombinase ORF and BGH polyA into the first coding exon of *Cd300c*. This strain description will be provided in a separate manuscript (Perez et al., in preparation) and is available upon request to B.R. For this study, *Cd300c*$^{Cre+/+}$ x *Rosa26*$^{TdTomato+/-}$ (CD300c^{TdT}) mice were used. Mixed bone marrow chimeras (BMC) were generated by lethally irradiating (two doses of 6Gy) 8-week-old females and transplanting with 3x10^6 BM cell suspensions (50% WT CD45.1 and 50% cKO CD45.2). BM cells were engrafted for ≥8 weeks. For DT inoculation, 50ng/g body weight was inoculated i.v. at day 0, followed by 25ng/g every other day. For BrDU experiments, 1 mg of BrDU (SIGMA) was inoculated i.p. at day 0, followed by continuous feeding with 0.8 mg/mL of BrDU in drinking water (prepared fresh daily). After 14 days, BrDU was removed and mice euthanized at different time points. For *in vivo* antigen uptake experiments, 1x10^8 sheep red blood cells (SRBCs) stained with 2μM PKH26 (Sigma-Aldrich) or 1x10^9 Yellow-Green Polystyrene Beads (Polysciences, Inc.) were injected i.v. for 3 hrs. For viral infection, 50 PFU M-CoV was injected i.p. In some experiments, M-CoV-infected mice were inoculated with 100 μg of anti-IL-1β or control Ab (BioXCell, clone B122 and Cat#BE0091, respectively) on day 2, or 200 μg of anti-NK1.1 or control Ab (BioXCell, clone PK136 and 2A3, respectively) on day −1, 0 and 2 post-infection. Animals were maintained in ventilated cages under specific pathogen-free conditions and a 12 hr dark:12 hr light cycle at 20-22°C and a humidity range of 30-70%. Animals were fed with Teklad Irradiated Rodent Diet (Inotiv #2918). Animals were used at 6-12 weeks of age in accordance with Stanford and New York University Administrative Panel on Laboratory Animal Care and overseen by the Institutional Animal Care and Use Committee.

Cell suspension preparation

Blood was obtained from anesthetized mice via retro-orbital puncture into a vial containing 1mM EDTA (Corning), and mononuclear cells were enriched using Lympholyte M (Cedarlane). Blood serum was used for measuring alanine 2-oxoglutarate-aminotransferase (ALT)(Sigma-Aldrich), or cytokines by Luminex (ThermoFisher; HIMC Stanford University). Spleens, peripheral LN (inguinal, brachial, and axillary) and perfused livers were digested with 400 U/mL Collagenase D (Millipore-Sigma) and 50 μg/mL DNase I (Millipore-Sigma) for 30 min at 37°C. 10 mM EDTA was added for the last 5 min of culture. For liver, leukocytes were enriched by density gradient centrifugation using 42% Percoll (Cytiva). Perfused lungs were digested with 0.13 U/mL Liberase TM (Millipore-Sigma) and 50 μg/mL DNase I for 25 minutes at 37°C. For BM, femurs and tibias were flushed using un-supplemented RPMI (Corning). All cell suspensions were filtered through

a 70 μm strainer. Red blood cells from spleen and BM were lysed using ACK Lysis buffer (Lonza).

Enrichment of DC and precursors

Mouse cell suspensions were incubated with anti-CD135-biotin (Biolegend) for 30 min at 4°C, washed and incubated with Ultra-Pure anti-Biotin microbeads (Miltenyi) for 30 min at 4°C. $CD135^+$ cells were selected using LS columns (Miltenyi). Human myeloid cells were negatively enriched from PBMCs using anti-CD3 (OKT3), anti-CD14 (HCD14), anti-CD19 (HIB19) and anti-CD335 (9E2) Abs followed by anti-mouse Dynabeads (Invitrogen) at a concentration of 4 beads per target cell[52]. For IL-1β experiments, human DC were negatively enriched using EasySep Human pan-DC Pre Enrichment Kit (StemCell Technologies).

Staining for flow cytometry and cell sorting

Abs (reporting summary) were purchased from Biolegend, R&D, MBL International and ThermoFisher. Anti-TCF4 (Abcam) was labeled in-house using the Alexa 647 Labeling Kit (ThermoFisher). Mouse cell suspensions were incubated with anti-CD16/CD32 (clone 2.4G2, produced in-house) to block non-specific binding for 15 min at 4°C. Cells were incubated with Ab cocktails in mouse FACS buffer (2 mM EDTA, 2% FBS in PBS) for 20 min at 4°C. DAPI (Sigma) was added to exclude dying cells before sample acquisition. For transcription factor staining, cells were stained with surface Abs and LIVE/DEAD Fixable Blue (ThermoFisher) in PBS for 20 min at 4°C, then fixed with FoxP3 Transcription Factor Fix/Perm Buffer (ThermoFisher) for 2-12 hrs and stained intracellularly for 30 min in 1X Permeabilization Buffer (ThermoFisher). For cytokines and EYFP co-staining, cells were surface stained and fixed with 2% paraformaldehyde (Electron Microscopy Sciences) for 40 min, followed by Cytofix/Cytoperm (BD Biosciences) for 12 minutes. Intracellular cytokine staining was performed in 1X Permwash (BD Biosciences) for 30 min. For BrDU staining, cells were surface stained, washed and fixed with Cytofix/Cytoperm for 30 min at 4°C, followed by incubation with Cytoperm Permeabilization Buffer Plus (BD Biosciences) for 20 min at 4°C and a second fixation with Cytofix/Cytoperm for 10 minutes at 4°C. Cells were then incubated with 160 U/mL DNase I for 1 hr at 37°C, followed by incubation with anti-BrDU PE (Biolegend) for 20 min at RT. For mouse cell sorting, lineage included Abs against CD3, CD19, NK1.1 and Ly6G for splenocytes plus MHCII for BM (all in Alexa700 or Efluor450), and streptavidin-Alexa647 to detect CD135 expression from CD135-enriched cells. Human PBMCs were incubated with human gamma-globulin (ThermoFisher) to block non-specific binding for 15 min at 4°C, followed by Abs in human FACS buffer (2 mM EDTA, 2% Donor equine serum in PBS) for 20 min at RT. For transcription factor staining, cells were stained with surface Abs and LIVE/DEAD Fixable Blue in PBS for 20 min at RT, fixed with FoxP3 Transcription Factor Fix/Perm Buffer for 1 hr at 4°C, and stained intracellularly for 20 min in 1X Permeabilization Buffer. Human tDC were sorted as lineage negative ($CD3^-CD19^-CD20^-CD335^-CD66b^-$), monocyte/DC3 negative ($CD14^-CD16^-$) and HLA-$DR^+CD123^+BDCA1^-AXL^+$ (using CD123 clone 6H6 to allow for IL-3 binding in culture). For IL-1β human experiments, pDC and tDC were sorted as HLA-$DR^+CD123^+AXL^-SIGLEC6^-$ and HLA-$DR^+CD123^+AXL^+SIGLEC6^+$, respectively. In all cases, analysis was performed in a 5-laser LSRFortessa X-20 (BD Biosciences), and

cell sorting in a FACSAria Fusion using BD Diva software (BD Biosciences), and SY3200 or SH800Z sorter and software (SONY Biotechnology). Data was analyzed using FlowJo (v.10.8.1; Tree Star, Inc). Unstained cells and single-fluorochrome-stained cells were used for accurate compensation. Control samples included fluorescence minus one.

Staining for CyTOF

Metal-labeled Abs (reporting summary) were obtained from Fluidigm or labeled using the MaxPar X8 labeling kit (Fluidigm). CD135-enriched mouse cell suspensions were stained with 0.25 μM cisplatin (Fluidigm) for 5 min at RT to exclude dead cells, washed with CyFACS buffer (2 mM EDTA, 1% BSA, 1% in PBS) and stained with a heavy-metal-labeled Abs for 30 min at 4°C. Cells were washed twice with CyFACS then fixed with Foxp3 Transcription Factor Fix/Perm Buffer for 2 hrs followed by intracellular staining in 1X Permwash for 30 min. After staining, samples were washed and incubated with 2% PFA in PBS containing 125 nM Iridium intercalator (Fluidigm) overnight. Cells were washed with water, filtered, and acquired. Human PBMC and sorted tDC were cisplatin and surface stained, followed by fixation as described above for mouse. The intracellular cocktail included Abs affected by fixation[52]. Sorted tDC were pooled with mouse splenocytes to avoid cell loss during washes[52]. In all cases, cells were acquired in a CyTOF2 or a Helios mass cytometer (Fluidigm) at the Shared FACS Facility at Stanford or Mt. Sinai, using CyTOF software.

Adoptive transfer experiments

10,000-30,000 cells sorted from 1-2 mice were adoptively transferred into WT congenic non-irradiated mice through tail vein injection. Analysis was performed 2-8 days later in the spleen. During analysis, splenocytes of recipient mice were enriched by density gradient centrifugation using 30% Bovine Serum Albumin (BSA, Millipore-Sigma)[4].

In vitro DC stimulation

$8x10^6$ mouse splenocytes were resuspended in 0.5mL of complete RPMI (complete medium contains: 10% FBS, GIBCO; 2 mM L-glutamine, Corning; 100 IU Penicillin, Corning; 100 mg/mL Streptomycin, Corning; 55 mM 2-Mercaptoethanol, GIBCO), and cultured for 6h at 37°C. Splenocytes were left untreated or stimulated with 200ng/mL LPS, 200ng/mL MPLA, 25μg/mL Poly(I:C), or 2.5μg/mL Resiquimod. For cytokine detection, 5 μg/mL Brefeldin A (Millipore-Sigma) was added to the culture. Costimulatory marker and cytokines were detected by surface and intracellular staining, respectively. $2x10^5$/mL purified splenic DC were incubated with M-CoV (MHV A59; MOI of 1) or mock control (supernatant from non-infected L929 cells) and cultured for 14-16 hrs at 37°C. IL-1β, TNF, IL-6 and IL-12p70 were measured by Cytometric Bead Array (CBA) Mouse Enhanced Sensitivity Flex Set and Mouse Enhanced Sensitivity Master Buffer Kit (BD Biosciences). Concentration of each cytokine was normalized to the mock control. Sorted human tDC were cultured in 96 well U-bottom plates at 37°C at a concentration of 5,000 cells in 200 μL complete RPMI. Media was supplemented with 10ng/mL IL-3 (R&D Systems) and 200ng/mL CD40L (R&D Systems) for 48 hrs. tDC phenotype was evaluated by CyTOF and flow cytometry. For IL-1β detection, enriched or sorted human DC were stimulated with 2.5 μM CpG-A (ODN 2216), MRC5, CMV-MRC5 and H1N1 influenza virus A/PR/8/34 (PR8) at 10 MOI for 6 to 9 hrs[41].

10 μg/ml of Brefeldin A (BFA) was added for the last 3-6 hours of incubation prior to flow cytometry and CyTOF experiments[41].

Bone marrow-derived DC

$2x10^6$ BM cells were plated in a 24-well plate with 2mL complete DMEM supplemented with 1.8mM sodium pyruvate (SIGMA), 1X MEM-NEAA (GIBCO #11140050), and 10% supernatant from B16-FLT3L cell line. In some cases, 1 mL of cell suspension was transferred at 3-days to a 24-well plate containing a mono-layer of mitomycin-treated OP9-DL1 cells[35]. At 4-7 days, cell suspensions were analyzed by flow cytometry. Lineage ($CD3^+$ and $CD19^+$) and macrophages ($SSC\text{-}A^{high}$ $F4/80^{high}$ cells) were gated out.

IgH D-J Rearrangement

Genomic DNA was isolated from sorted DC using the Nucleospin Tissue XS kit (Takara Bio). The amount of DNA per reaction was equalized by qPCR using primers against *Actb*[4]. The primers used were as follows: *Actb* forward 5'-GGTGTCATGGTAGGTATGGGT-3', reverse 5'-CGCACAATCTCACGTTCAG-3'; Mu0-J_H1 (germline) forward 5'-CCGCATGCCAAGGCTAGCCTGAAAGATTACC-3', reverse 5'-GGTCCCTGCGCCCCAGACA-3'; D_HL-J_H3 forward 5'-TGGCAGGGATTTTTGTCAAGGGATCTACTACTGTG-3', reverse 5'-CTAATTCTCACAAGAGTCCGATAGACCCTGG-3'. Products were run on a 2% agarose gel and imaged with a ChemiDoc MP (Bio-Rad).

In vitro T cell activation

Spleen, skin draining LN, mesenteric LN, and iliac LN of OT-II mice were collected and mechanically dissociated. Cells were lysed using ACK Lysis buffer (Lonza), filtered through a 70 μm strainer, and incubated with Abs against B220, F4/80, MHCII, NK1.1 and CD8 (produced in-house) for 30 min at 4°C followed by sheep anti-Rat IgG Dynabeads (Invitrogen). Negatively enriched $CD4^+$ T cells were labeled with 5 μM CellTrace Violet (CTV, ThermoFisher), and naïve T cells sorted as $CD3^+CD4^+CD44^{lo}CD45RB^+$. Naïve T cells were cultured with sorted splenic DC (1:5 ratio) and 20 μg/mL ovalbumin (OVA) for 4 days. Controls included T cells incubated with OVA in the absence of DC.

Viral stocks and titers

Influenza virus H1N1 (PR8), CMV stocks and infected cell lines were previously generated[41]. Thawed MRC5 and CMV-MRC5 were plated at the density of $6x10^4$ cells/cm^2 for > 8 hrs before the addition of $5x10^3$ - $4x10^4$ human DC. M-CoV (also known as murine hepatitis virus, MHV A59; BEI Resources) was propagated on L929 cells (ATCC). M-CoV viral titers were determined after homogenization by standard plaque assay using L929 cells.

Transcriptomic data generation

For bulk-RNAseq, splenic DC from 2 mice were CD135-enriched and split in two samples: 30% was stained to sorting, and 70% was stimulated with the LPRC adjuvant cocktail [100ng/mL LPS, 25μg/mL Poly(I:C), 2.5μg/mL Resiquimod and 6μg/mL CpG-A (ODN 2216)] at a concentration of 10^7/mL for 3 hrs before staining and sorting. RNA was

extracted using the NucleoSpin RNA XS kit (Takara Bio). For scRNAseq, CD135-enriched cells were stained and sorted. Splenocytes were mixed 1:1 from 2 sorted gates to enrich for tDC: $CD3^{-}CD19^{-}NK1.1^{-}Ly6G^{-}$ and $CD3^{-}CD19^{-}NK1.1^{-}Ly6G^{-}XCR1^{-}CD11b^{lo}$ (Fig.1c). BM cells were sorted as $CD3^{-}CD19^{-}NK1.1^{-}Ly6G^{-}$. 600 sorted cells per μL were processed for 10X Genomics. For NanoString, sorted DC were resuspended in 1/3 RNeasy Lysis Buffer RLT (Qiagen) at a concentration of 1,000-5,000 cells/μL and analyzed on the NanoString nCounter® Mouse Myeloid Innate Immunity V2 Standard Platforms, following the manufacturer's instructions. Samples were processed on the NanoString Digital Analyzer to yield a reporter code count (RCC) dataset, which was analyzed *via* ROSALIND® (https://rosalind.bio).

CyTOF data analysis

Files in FCS format were normalized with the R package Premessa. Mouse splenocytes were gated as live/singlets/$CD3^{-}$/$CD19^{-}$/$CD335^{-}$/$Ly6G^{-}$, exported, and analyzed by UMAP and X-shift in FlowJo. Analyzed files were imported into MATLAB (v.9) for visualization. MEM was performed following R scripts[53]. The Scaffold R package was downloaded from GitHub (https://github.com/nolanlab/scaffold)[54]. Human DC were gated from PBMC in FlowJo and imported into Scaffold to create a reference map. Events from stimulated tDC were imported into the reference map for clustering[29].

Bulk-RNAseq analysis

The count matrix was generated using the “Seq-N-Slide” pipeline (https://github.com/igordot/sns). Data was aligned using STAR (v2.7.3a) to the mm10 reference genome. featureCounts was used to generate the gene-count matrix. The count matrix was analyzed using DESeq2 (v3.14)[55]. Differential gene expression analysis was performed using DESeq2’s DESeq function. Log fold change shrinkage was performed by the “ashr” method[56] and used for volcano plots and MA plots (DESeq2)[55]. Variance stabilizing transformation was performed using DESeq2 for heatmap and PCA visualization.

scRNAseq analysis

Cell Ranger (10x Genomics) was used for demultiplexing and generation of barcodes and count matrices. Spleen and BM data were analyzed using Seurat (v3)[57] in R (4.1.2). Cells were selected for number of genes over 300, number of total counts less than 50000, and % of mitochondrial genes less than 20%. Data was normalized using the “LogNormalize” method (scale factor 10000) of Seurat’s NormalizeData function. PCA was performed in Seurat and the top 25 dimensions were used for UMAP. Differentiating markers for each cluster were identified using the Wilcoxon rank sum test implemented in Seurat’s FindAllMarkers function (min.pct=0.25, logfc.threshold =0.25). KNetL graphs were generated using iCellR (v1.6.5)[58]. Cells were filtered for <20% mitochondrial genes, unique genes expressed between 300-8000 genes, and UMIs less than 50,000. Monocytes were filtered using cell IDs of cells in Cluster 9 from the spleen UMAP analysis in Seurat. Data was normalized using the default “ranked.glsf” method in iCellR. PCA was calculated using the top 2000 genes. KNetL analysis was performed using 1:20 dimensions with a zoom of 175 and UMAP as the dimensionality reduction method. Clusters were calculated using the KNetL results with a sensitivity of 150. Differential gene expression

was calculated for each cluster using the findMarkers function of iCellR with default parameters except with adjusted p-value <0.05 set as the threshold of significance.

GSEA analysis

For bulk-RNAseq, a gene list was created by ranking all genes post log fold change shrinkage by the log_2FC value. The mouse hallmark gene set was downloaded (MSigDB website)[59,60] and used as the input for gene sets database. GSEAPreranked analysis was run on GSEA (v4.2.2) with 1000 permutations. For scRNAseq, a ranked gene list was created by computing markers for each cluster using Seurat's FindMarkers with min.pct and logfc.threshold parameters set to 0 to extract all genes. Genes were then ranked on the logFC value and analyzed using the same parameters as above.

Cell type signature generation

CPM counts from the sorted populations of the bulk-RNAseq were used to generate a signature matrix using CIBERSORTx with default parameters[61]. The signature matrix was then used to calculate signature scores for each cell of the spleen scRNA sequencing using the imputing cell fraction function of CIBERSORTx (permutations = 500, B-mode batch correction). Raw counts for tDC, pDC, DC1, and DC2 from the spleen scRNAseq were used to generate a signature matrix using CIBERSORTx with default parameters. The signature matrix was then used to calculate signature scores for each cell of the BM scRNAseq by imputing cell fraction (CIBERSORTx) (permutations = 500). pDC-signature "high" cells were defined as signature score >0.15.

Trajectory analysis

BM cells with pDC signature >0.15 were selected and re-clustered using Seurat. UMAP was generated using the top 25 statistically significant PCA components. Trajectory analysis was performed on UMAP embeddings from Seurat clustering using Slingshot (v2.2.0)[62]. For RNA velocity analysis, Velocyto (0.17.17)[63] was used to generate the loom file containing spliced and un-spliced transcripts. The mask file, mm10_rmsk, was downloaded from the UCSC genome browser. The genome annotation file, mm10_2020_A, was downloaded from 10x Genomics. The data was then loaded into scVelo (v.0.2.4)[63,64] for further analysis using Python (v3.10). scVelo was run with default settings using the "filter_and_normalize" and "moments" functions to filter and compute PCA/nearest neighbors, respectively. Results were overlayed onto Seurat-clustered UMAP of the BM.

Statistical analysis

For Fig.1-7 experiments, no statistical methods were used to predetermine sample sizes. For Fig. 8, the number of mice was estimated using power analysis (G*Power 3). Data distribution was assumed to be normal, but this was not formally tested. Individual experiments used mice of the same sex and age, without randomization. Data collection and analysis were not performed blinded. No data points were excluded. For scRNAseq, pre-established criteria for single-cell exclusion, i.e., low number of unique genes, abnormally high read count, and high mitochondrial gene content, was used. Statistical details of experiments, including statistical tests used, n value, number of experiments, and the type

of statistical tests can be found in figure legends. Statistical analysis was performed with at least three biological replicates using GraphPad Prism 9 (GraphPad Software) or R (v.4.1.2) statistical programming language. All graphs show mean +/− SD. gMFI indicates geometric mean fluorescence intensity. Graphics created with BioRender.com.

Extended Data

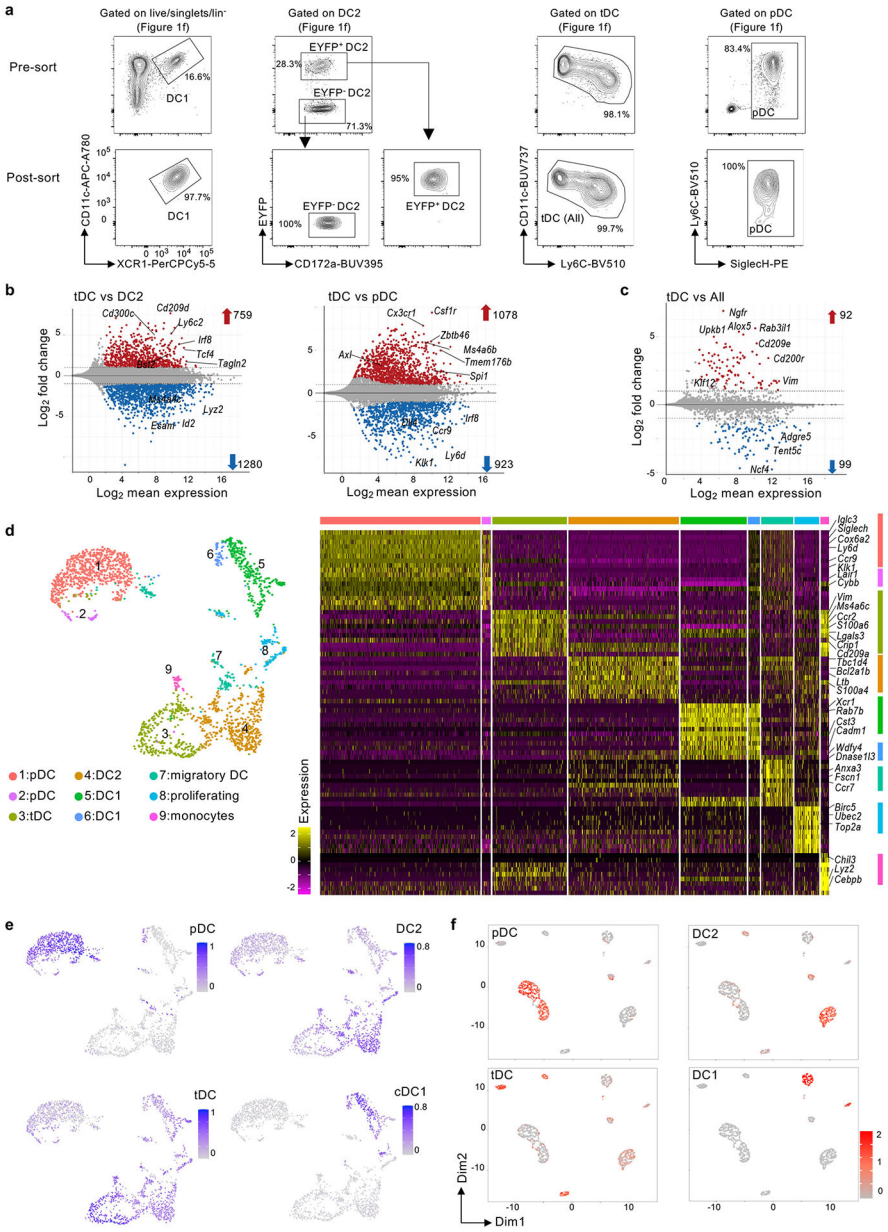

Extended Data Fig. 1. tDC are distinct transcriptionally.

a. CD135-enriched splenocytes from hCD2^{EYFP} mice were stained and sorted. Briefly, lineage containing CD3^{+}/CD19^{+}/NK1.1^{+}/Ly6G^{+} cells were removed, and cells were gated using the strategy described in Fig.1f. DC2 were further separated as EYFP^{+} and EYFP$^{−}$ cells. Shown are cells before (upper panels) and after sort (bottom panels).

b. MA plots of bulk-RNAseq data comparing tDC vs DC2 and tDC vs pDC. Genes with 2-fold Log_2 change are shown in red (up) and blue (down) (see also Supplementary Table S4).

c. MA plot comparing tDC vs all other DC (pDC, DC2 and DC1). Genes with 2-fold Log_2 change are shown in red (up) and blue (down) (see also Supplementary Table S1).

d. scRNAseq of splenic DC subsets. Splenic DCs were sorted as shown in Fig.1c and sequenced using droplet-based genomics. After filtering, 2,110 cells were analyzed. UMAP of clusters detected using Seurat's pipeline (right). Heatmap of top DEG between clusters (left).

e. DC signature scores generated using CIBERSORTx in the bulk-RNAseq data from (a) was overlayed on UMAP from (d).

f. As in (e), but DC signature scores were overlayed on the KNetL Plot from Fig.1d.

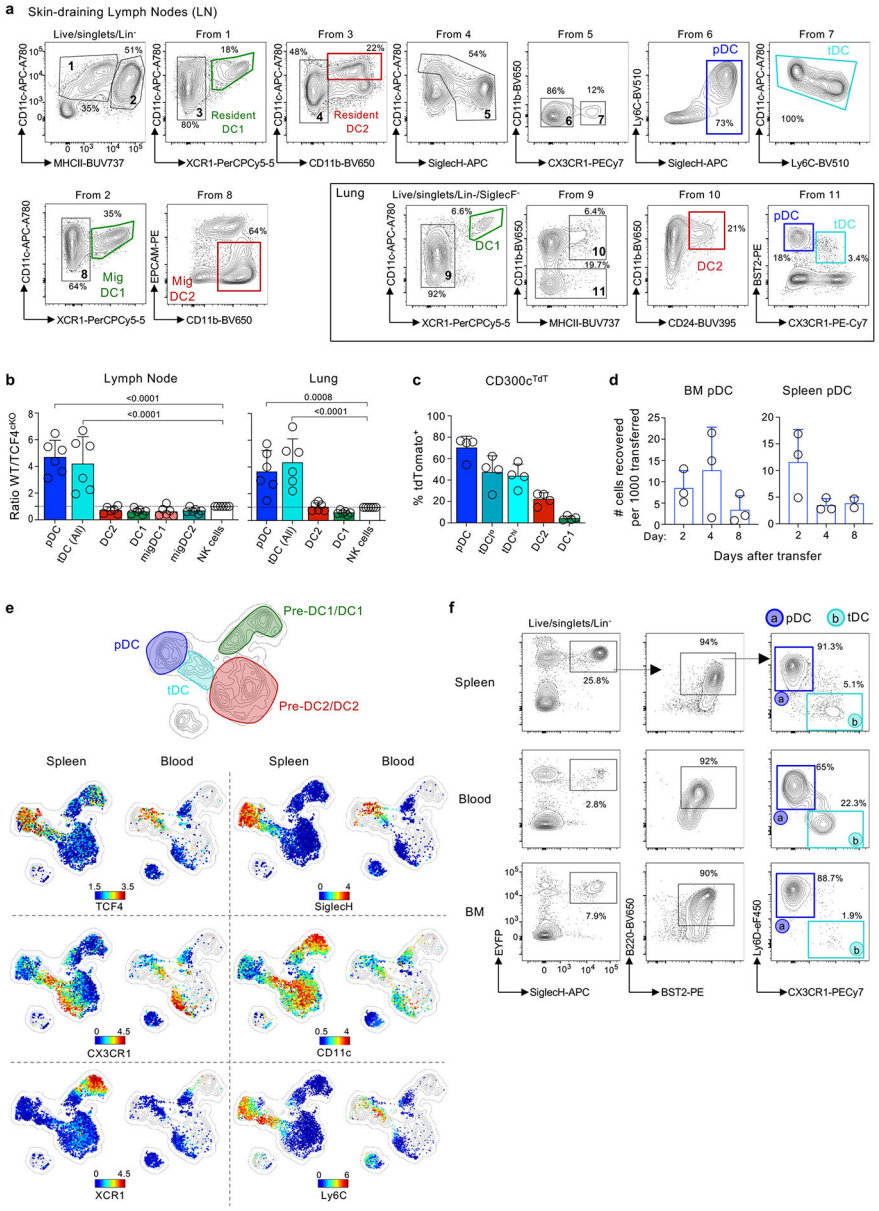

Extended Data Fig. 2. tDC originate from BM progenitors.

a. Gating strategy used for the analysis of skin-draining lymph node (LN) and lung DC subsets excluded. Lineage contains $CD3^+/CD19^+/NK1.1^+/Ly6G^+$ cells.

b. Bar graphs (mean + SD) showing the contribution of donor cells to LN and lung DC populations (gated as in (a)) in mixed BMC generated by transplanting 50% CD45.1 WT and 50% CD45.2 $TCF4^{cKO}$ BM, normalized to NK cells (n=6 mice in 2 experiments). Statistics determined by two-way ANOVA with Dunnett's multiple comparison test.

c. Bar graph (mean + SD) showing the percentage of splenic DC (gated as in Fig.1f) labeled with the lineage tracing $CD300c^{TdT}$ (n=4 mice in 3 experiments).

d. Adoptive cell transfer of 30,000 BM (left) or splenic (right) $CX3CR1^{EGFP}$ CD45.1 pDC into CD45.2 WT non-irradiated congenic mice. Recipient mice were euthanized at different time points (2-8-days) and the number of recovered cells (gated on $CD45.1^+$ and $CX3CR1^+$)

calculated per 1000 cells transferred (mean + SD). N=3/time point except n=2 for splenic pDC at 8-days. N represents number of mice and experiments.

e. CyTOF analysis of blood and spleen DC, analyzed by UMAP. Cells were gated as $CD3^{-}CD19^{-}NK1.1^{-}Ly6G^{-}$. Populations were delineated manually (top) and colored by marker expression (bottom)(n=2 mice in 2 experiments).

f. Spleen, blood and BM of $hCD2^{EYFP}$ mice were analyzed for the presence of $EYFP^{+}$ cells, that were further separated in $Ly6D^{+}$ pDC and $CX3CR1^{+}$ tDC. Lineage includes $CD3^{+}/CD19^{+}/NK1.1^{+}/Ly6G^{+}$ cells. One representative of 3 experiments.

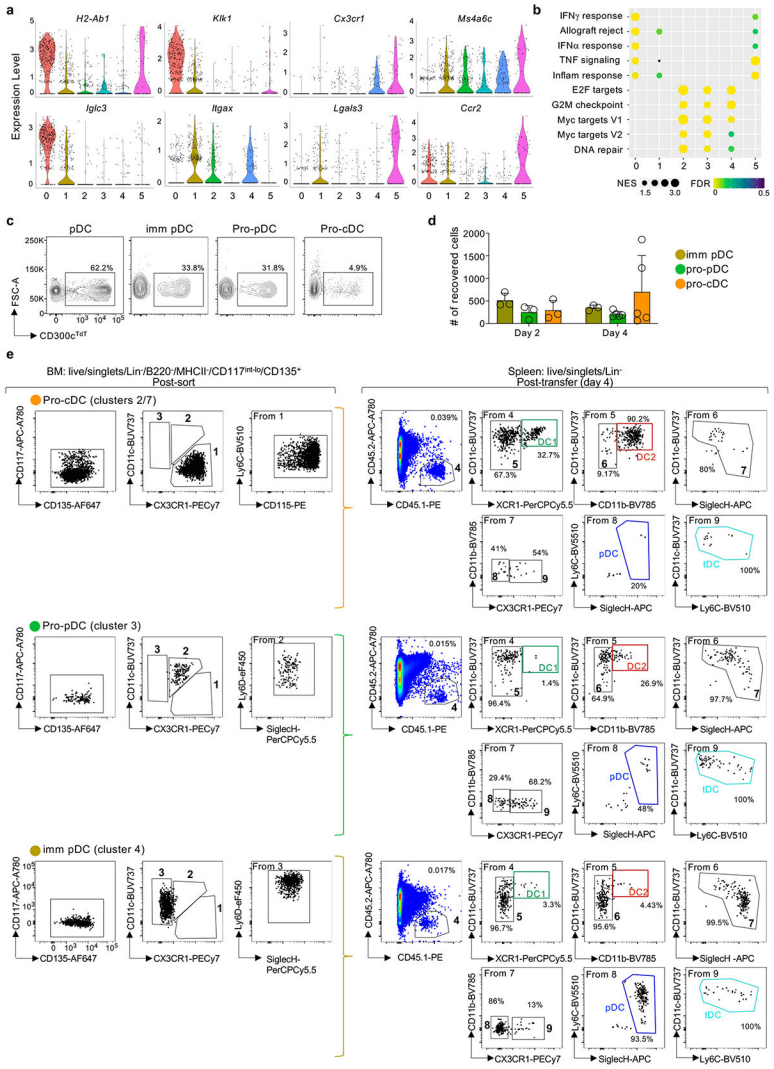

Extended Data Fig. 3. tDC originate from pro-pDC.

a. $CD135^{+}$ BM cells were enriched, sorted as $CD45^{+}/CD3^{-}/CD19^{-}/Ly6G^{-}$, and prepared for scRNA-seq. Cells with a pDC-specific gene enrichment score of >0.15 were selected and re-clustered using Seurat as shown in Fig.3d. Violin plots show the expression of the indicated genes in the clusters defined in Fig.3d.

b. As in (a) but GSEA of selected pathways from clusters defined in Fig.3d. Bubble size indicates the normalized enriched score (NES), and color scale depicts False Discovery Rate (FDR).

c. TdTomato expression in bone marrow progenitor cells from CD300c^{TdT} mice, gated as in Fig.3j. One representative experiment.

d. Imm pDC, pro-pDC and pro-cDC from the BM of CX3CR1^{EGFP} or hCD2^{EYFP} CD45.1 mice were purified as described in Fig.3j and transferred into CD45.2 WT mice. 2- and 4-days post-transfer, recipient mice were analyzed for transferred cells in the spleen. Shown is the number of cells recovered in the spleen of recipient mice (mean + SD). Imm pDC: n=3 at 2- and 4-days. Pro-pDC: n=3 at 2-days, and n=5 at 4-days. Pro-cDC: n=3 at 2-days, and n=5 at 4-days. N represents number of mice and independent experiments.

e. BM cells from CX3CR1^{EGFP} or hCD2^{EYFP} CD45.1 mice were CD135-enriched and purified by cell sorting using the gating strategy shown in Fig.3j. Purified progenitors were adoptively transferred into congenic non-irradiated CD45.2 WT mice and analyzed 4-days later in the spleen of recipient mice. Left panels show post-sort purity of progenitors. Right panels show transferred cells recovered in the spleen of recipient mice, analyzed using the gating strategy described in Fig.1f. In both cases, lineage includes CD3$^+$/CD19$^+$/CD335$^+$/Ly6G$^+$ cells. One representative of ≥ 3 experiments.

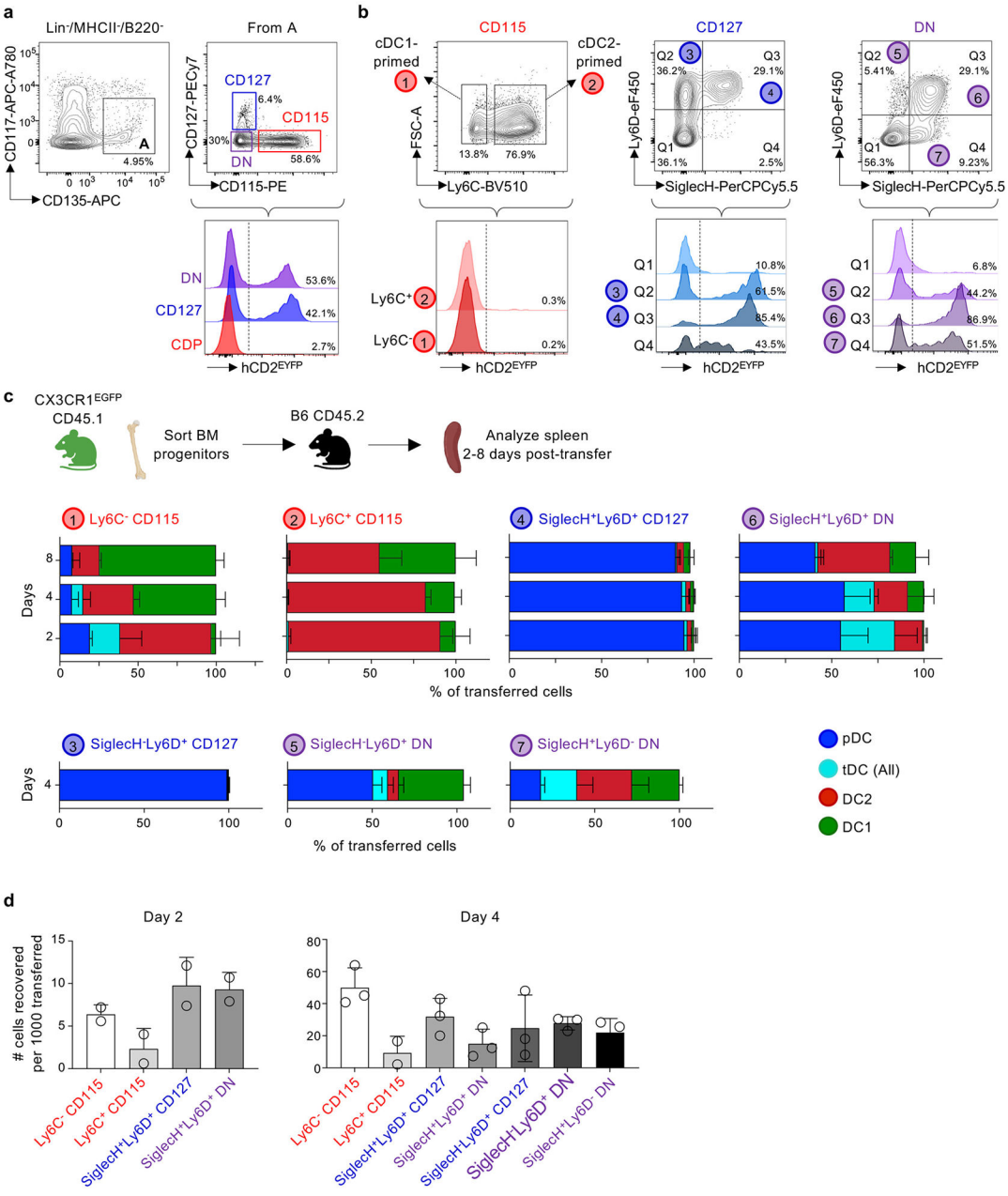

Extended Data Fig. 4. tDC originate from DN progenitors.

a. Gating strategy of CD135-enriched BM progenitors from hCD2^{EYFP} mice. Cells were stained for flow cytometry. Lineage contain CD3$^+$/CD19$^+$/NK1.1$^+$/Ly6G$^+$ cells. EYFP labeling is shown in the lower panels. One representative of 3 experiments.

b. As in (a), but CD115 progenitors were further gated based on the expression Ly6C, whereas CD127 and DN progenitors were gated based on the expression of Ly6D and SiglecH (top). Bottom histograms show EYFP expression in each population. One representative of 3 experiments.

c. The schematic shows adoptive transfer of 15,000-30,000 from CX3CR1^{EGFP} CD45.1 BM progenitors into WT CD45.2 non-irradiated congenic mice. Transferred cells were identified

in the spleen of recipient mice as CD45.1^{+} and CX3CR1^{+} cells. Bar graphs (mean + SD) show the percentage of each population recovered in the spleen (gated as shown in Fig.1f). N ≥ 2/mice and experiments.

d. As in (c), but bar graphs (mean + SD) number of cells recovered in the spleen of recipient mice. N represents number of mice and independent experiments.

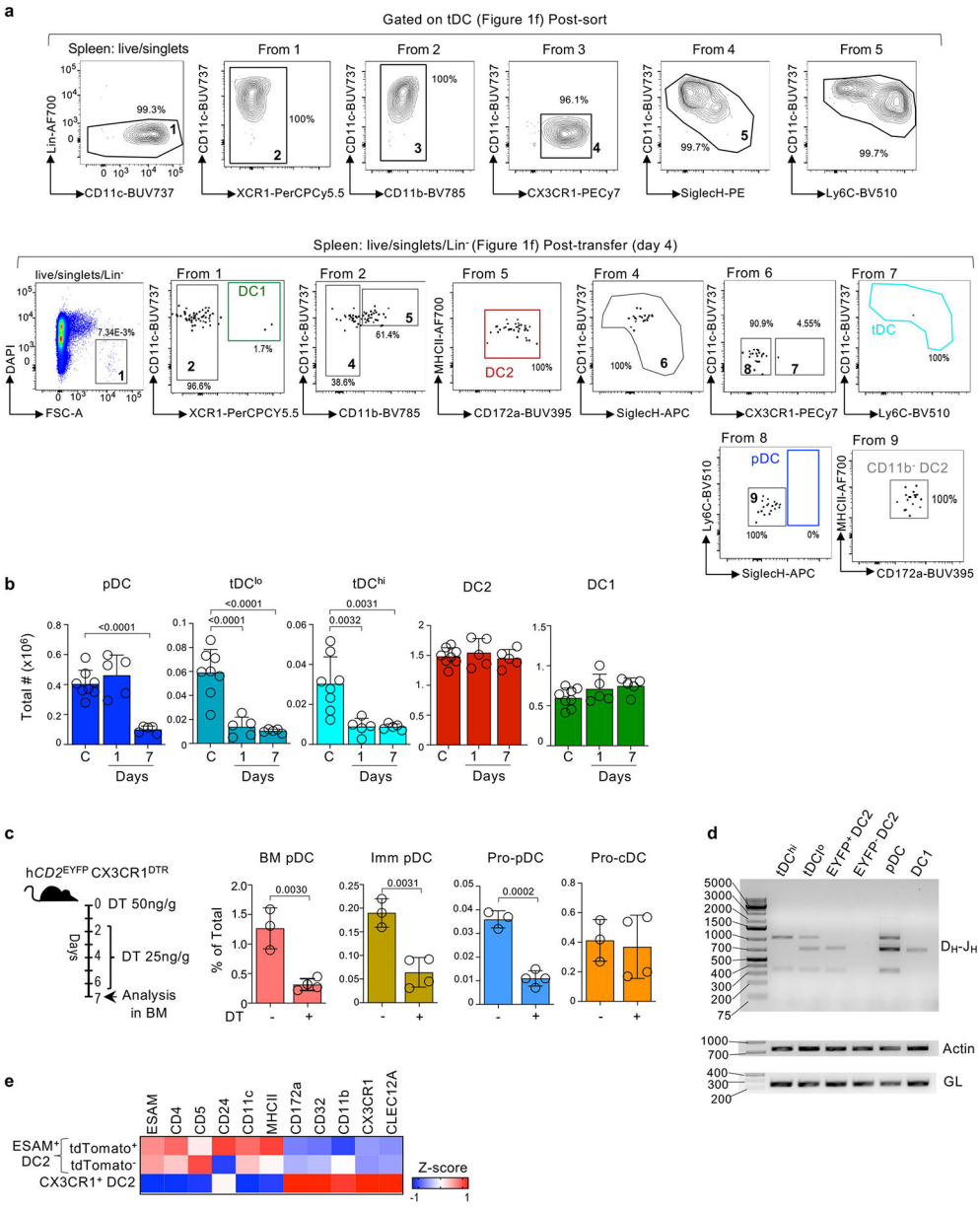

Extended Data Fig.5. tDC convert into DC2.

a. tDC were purified using the gating strategy described in Fig.1f. Top graph shows cell purity after sort. Bottom graphs show the outcome of transferred cells in the spleen of recipient mice analyzed at 4-days. One representative of 6 experiments.

b. Bar graphs (mean + SD) of the total number of splenic DC in h*CD2-i*Cre$^{+/-}$ *Cx3cr1*$^{DTR+/-}$ mice inoculated with DT and analyzed 1 day after (n=5 mice in 4 experiments), or

inoculated with DT every second day and analyzed 7 days later (n=5 mice in 4 experiments). "C" represents control mice (n=8 mice in 4 experiments), which are a combination of h*CD2-i*Cre$^{-/-}$ *Cx3cr1*$^{DTR+/-}$ mice inoculated with DT or h*CD2-i*Cre$^{+/-}$ *Cx3cr1*$^{DTR+/-}$ mice inoculated with PBS (no differences were observed between these control mice). Statistics determined by one-way ANOVA with Tukey's multiple comparison test.

c. As in (b), but BM progenitors from hCD2^{EYFP} CX3CR1^{DTR} mice were analyzed after 7 days of DT inoculation (n=4 mice). Control mice are hCD2^{EYFP} CX3CR1^{DTR} mice inoculated with PBS (n= 3 mice). Bar graphs (mean + SD) of the frequency of total progenitor populations from Fig.3j. Data pooled from 2 experiments. Statistical differences were determined by unpaired two-tailed t-test.

d. Mouse splenic DC subsets were sorted using the gating strategy show in Fig.1f and Fig.4g, and analyzed by PCR assay for IgH D-J rearrangements. Actin and IgH germline (GL) are also shown. One representative of 3 experiments.

e. DC2 from CD300c^{TdT} mice were gated as indicated in Fig.4f, and further separated in TdTomato^{+} and TdTomato^{-}. Heatmap indicating the relative expression (Z-score of gMFI) of surface markers. Z-score was calculated base of n=2 mice in 2 experiments.

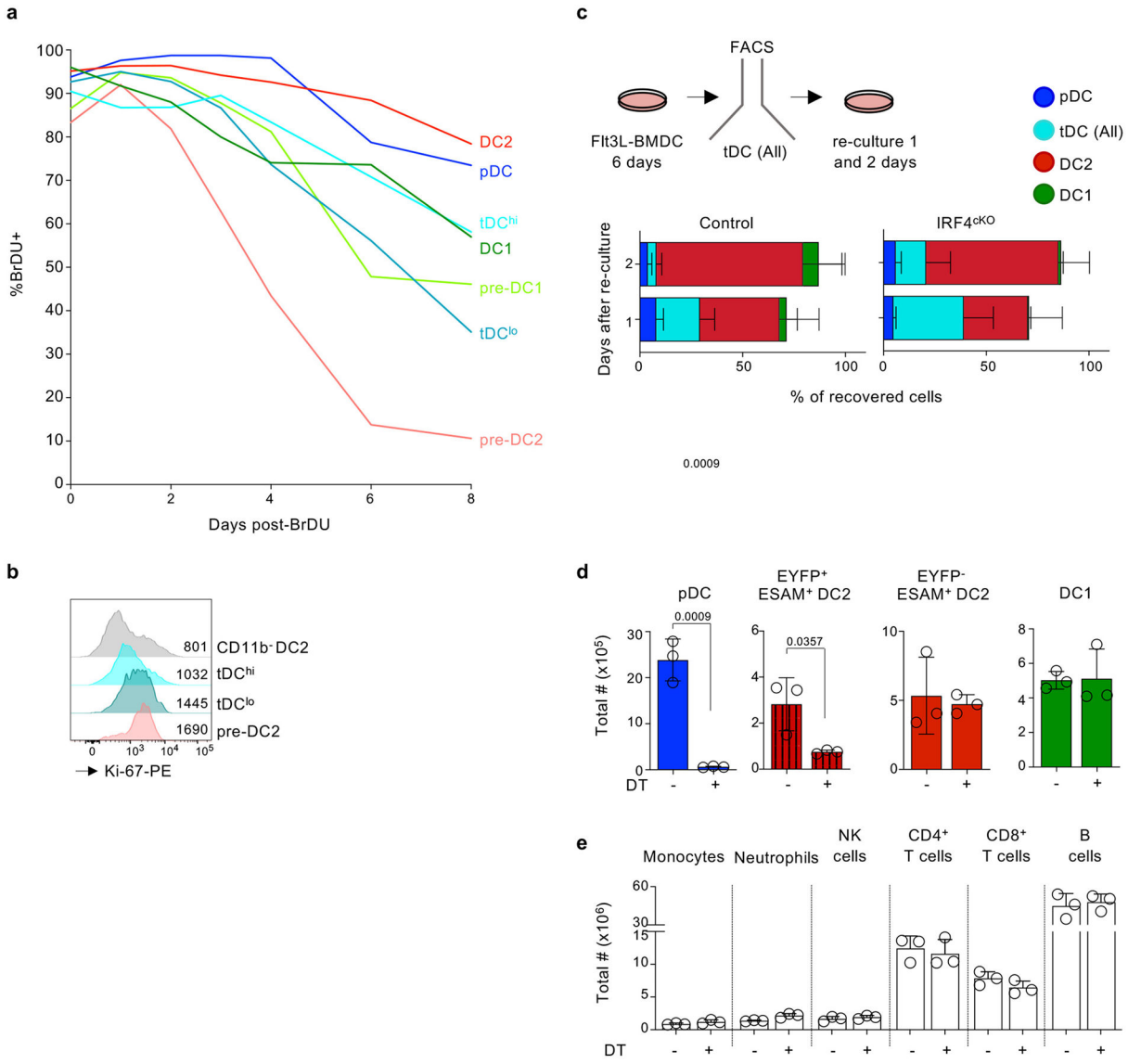

Extended Data Fig. 6. tDC have lower turnover rate than pre-DC2 and required IRF4.

a. Mice were inoculated i.p. with 1 mg of BrdU on day 0 and then fed continuously for 14 days with 0.8 mg/mL of BrdU in drinking water. After 14 days, BrDU was removed. Mice were euthanized at different time points post-BrdU removal, spleen cell suspension prepared and stained for BrdU and the identification of DC subsets as described in Fig.1f and Fig.5e. N ≥ 2/mice per time point in 2 independent experiments.

b. Expression of Ki-67 in each splenic DC population gated as described in Fig.1f and Fig.5e, analyzed by flow cytometry. One representative of 3 experiments.

c. BM cells from IRF4^{cKO} or IRF4^{control} mice were cultured with FLT3L as described in Fig.2c. At day 6, tDC were sorted and re-cultured in complete media and 1% FLT3L for 1 and 2 days. Bar graphs (mean + SD) show the percentage of each DC recovered. N=3 biologically independent samples in 3 experiment.

d. Bar graphs (mean + SD) of the total number of splenic DC (gated a Fig.1f and Fig.4f) in hCD2^{EYFP} CX3CR1^{DTR} mice inoculated with DT every second day (n=3 mice) or left

untreated (n=3 mice), and analyzed at day 10. Statistics determined by unpaired two-tailed t-test.

e. As in (d), but shown is the number of other immune cells.

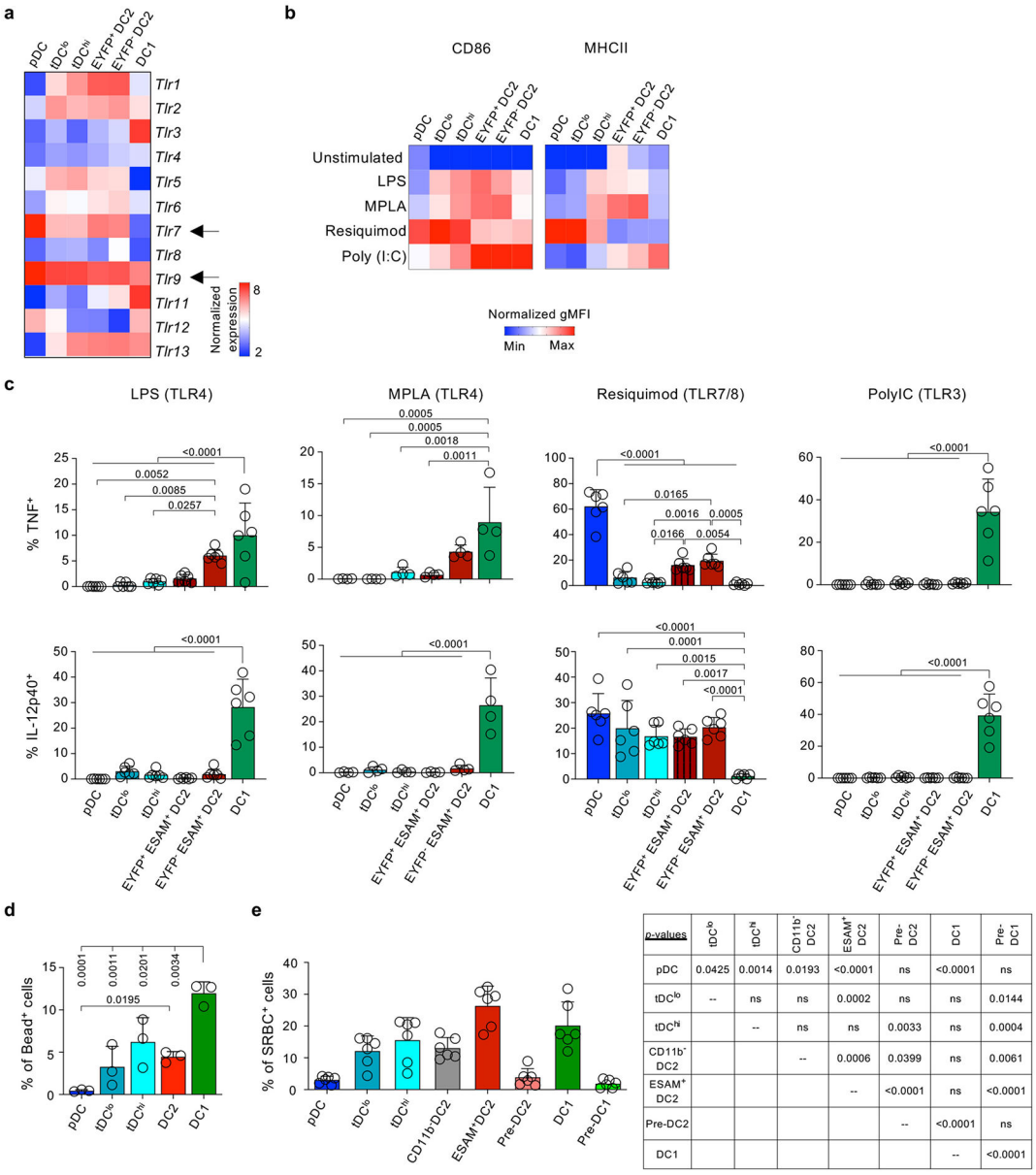

p-values	tDC^{lo}	tDC^{hi}	CD11b$^-$ DC2	ESAM$^+$ DC2	Pre-DC2	DC1	Pre-DC1
pDC	0.0425	0.0014	0.0193	<0.0001	ns	<0.0001	ns
tDC^{lo}	--	ns	ns	0.0002	ns	ns	0.0144
tDC^{hi}		--	ns	ns	0.0033	ns	0.0004
CD11b$^-$ DC2			--	0.0006	0.0399	ns	0.0061
ESAM$^+$ DC2				--	<0.0001	ns	<0.0001
Pre-DC2					--	<0.0001	ns
DC1						--	<0.0001

Extended Data Fig. 7. tDC respond to microbial stimulation and uptake antigen *in vivo*.

a. Splenic DC subsets purified as described in Fig.1f and Fig.4f were analyzed by Nanostring. Heatmap shows the expression of TLRs by each DC subset. N=2 mice in 2 experiments.

b. Whole spleen cell suspensions were activated with LPS, MPLA, Resiquimod or PolyIC for 6 hrs. Heatmap showing the upregulation of MHCII and CD86 in pDC, tDC, ESAM$^+$ EYFP$^+$ and EYFP$^-$ DC2, and DC1. Min and max correspond to the lowest and highest gMFI per row, respectively. N=6 mice per group. Data pooled from 4 experiments.

c. As in (b), but bar graphs (mean + SD) of cytokine production. Whole spleen cell suspensions were activated with LPS (n=6), MPLA (n=4), Resiquimod (n=6) or PolyIC (n=6) for 6 hrs. TNF and IL-12p40 were detected by intracellular cytokine staining. N represents mice and data was pooled from 4 experiments. Statistical differences were determined by One-way ANOVA with Tukey's multiple comparisons test.

d. Mice were inoculated with yellow-green polystyrene (YG-PS) beads i.v. Three hrs later, spleens were harvested and the phagocytosis of the particle was assessed by flow cytometry in each DC population, gated as in Fig.1f (n=3 mice in 3 experiments). Bars represent mean + SD. Statistical differences were determined by One-way ANOVA with Tukey's multiple comparisons test.

e. As in (d), but mice were inoculated with PKH26-labeled SRBC (n=6 mice in 4 experiments).

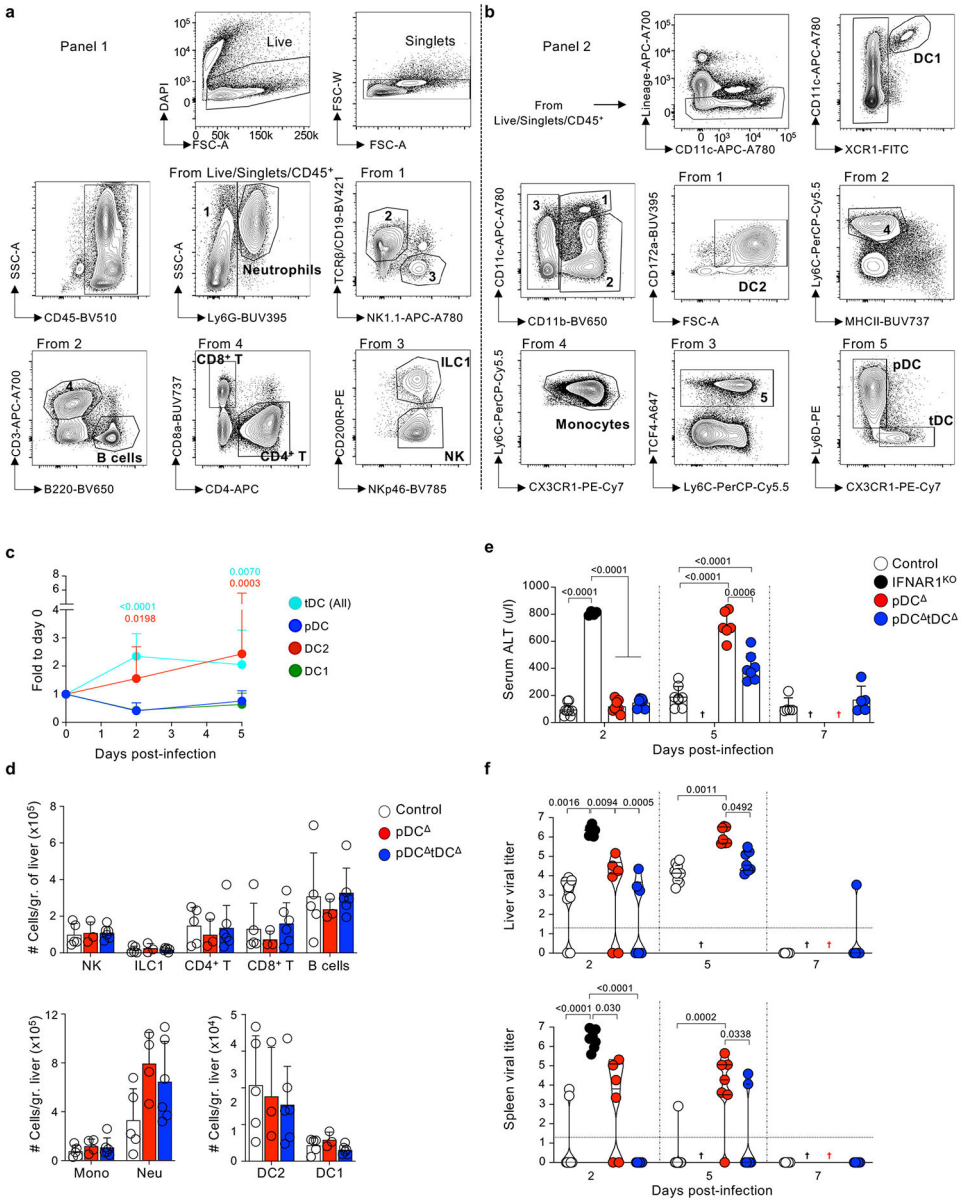

Extended Data Fig. 8. Number of immune cells, viral titer and ALT in pDC- and pDC/tDC-depleted animals infected with M-CoV.

a. Liver cell suspensions were enriched in immune cells using a Percoll gradient, and stained with a cocktail of Ab for the analysis of neutrophils and lymphocytes. One representative of 3 experiments.

b. As in (b), but cell suspensions were stained for the analysis of DC and other myeloid cells. Lineage contains $CD3^+/CD19^+/NK1.1^+/Ly6G^+$ cells. One representative of 3 experiments.

c. Liver of WT mice were analyzed for the number of DC subsets by flow cytometry 2- and 5-days post-M-CoV infection. Fold change of the number of each subset to day 0 is shown. N=3 at 0 days, n=14 at 2-days, and n=11 at 5-days. Data pooled from ≥ 4 experiments. p-values represent statistical differences between tDC and DC2 vs DC1.

d. Liver immune cell numbers 2-days post-M-CoV infection of pDC^{Δ} (n=3); $pDC^{\Delta}tDC^{\Delta}$ (n=6) and control (n=5) mice. pDC^{Δ} mice are *BDCA2*-$DTR^{+/-}$ mice inoculated with DT one day before M-CoV infection. $pDC^{\Delta}tDC^{\Delta}$ are $hCD2^{EYFP}$ $CX3CR1^{DTR}$ mice inoculated with DT every other day for 5-days before M-CoV infection. Control mice are a combination of *BDCA2*-$DTR^{+/-}$ or $hCD2^{EYFP}$ $CX3CR1^{DTR}$ mice inoculated with PBS, and $DTR^{-/-}$ mice inoculated with DT (no difference in control mice was observed). Shown is mean + SD. N represents independent mice in 2 experiments.

e. As in (d), but serum ALT values (mean + SD) were determined 2-, 5- and 7-days post-M-CoV infection. N ≥ 4 mice/group/time point in 4 experiments.

f. As in (e), but viral titers (log_{10} pfu/gr. Tissue) in liver (top) and spleen (bottom) were determined 2-, 5- and 7-days post-M-CoV infection. N ≥ 4 mice/group/time point. Violin plots show distribution of data pooled from 4 exp.

Statistical differences determined by Two-way ANOVA with Tukey's multiple comparisons test (c,e,f), or One-way ANOVA with Tukey's multiple comparisons test per subset (d).

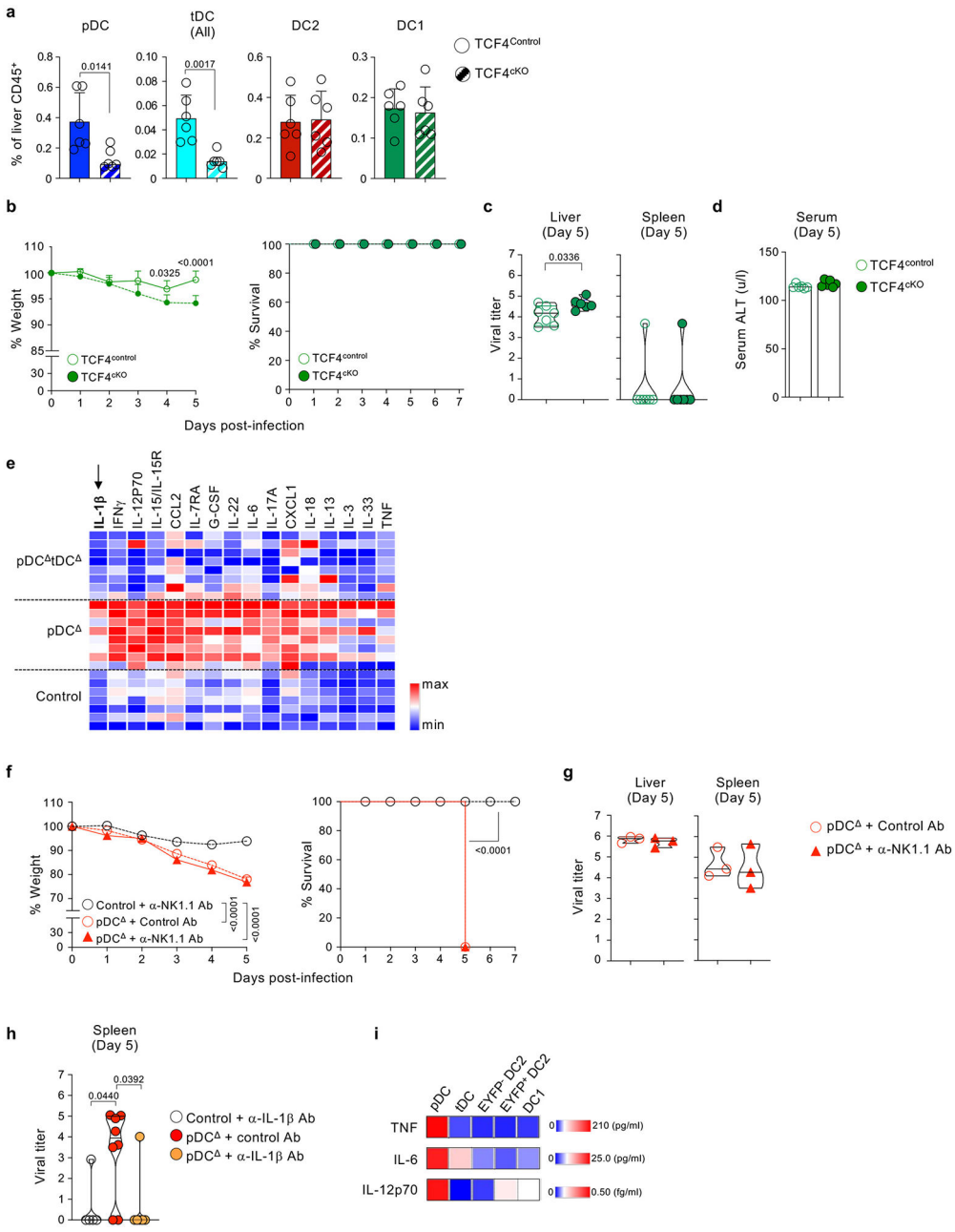

Extended Data Fig. 9. tDC promote immune pathology following M-CoV infection.

a. TCF4^{cKO} vs TCF4^{control} mice were generated by transplanting *Itgax*-Cre$^{+/-}$ Tcf4$^{fl/fl}$ or *Itgax*-Cre$^{-/-}$ Tcf4$^{fl/fl}$ BM into lethally irradiated CD45.1 WT mice, respectively. 2 months post-reconstitution, mice were infected with M-CoV, and the frequency of liver DC (mean + SD) analyzed 2-days later (n=6 mice/group in 2 experiments).

b. Percentage weight loss (left, mean + SD) and survival (right) of TCF4^{cKO} (n=7) vs TCF4^{control} (n=10) mice in 3 experiments.

c. As in (b), but viral titers (log_{10} pfu/gr. tissue) were determined 5-days post-M-CoV infection. N=7 mice for TCF4^{control} and n=6 mice for TCF4^{cKO}. Violin plots show distribution from 3 experiments.

d. As in (b), but shown is serum ALT (mean + SD; n=6 mice/group in 3 experiments).
e. Serum cytokines were determined by Luminex in control (n=7 mice), pDC$^{\Delta}$ (n=8) and pDC$^{\Delta}$tDC$^{\Delta}$ (n=8) 2-days p.i. in 4 experiments. Shown are cytokines significantly different between pDC$^{\Delta}$ vs pDC$^{\Delta}$tDC$^{\Delta}$ mice.
f. Percentage weight loss (left, mean + SD) and survival (right) of pDC$^{\Delta}$ mice inoculated with anti-NK1.1 Ab or isotype control on day -1, 0 and 2 post-infection with M-CoV. N=3 mice/group except n=5 mice for pDC$^{\Delta}$ + isotype, pooled from 2 experiments.
g. As in (f), but viral titers were evaluated at 5-days p.i. (n=3 mice/group). Violin plots show distribution from 2 experiments.
h. As in Fig.8j, but splenic viral titers (log_{10} pfu/gr. tissue) were determined. N=5 mice/group except n=8 for pDC + control Ab. Violin plots show distribution from 2 experiments.
i. As in Fig.8k but heatmaps show secretion of TNF, IL-6 and IL-12p70 by DC subsets (N=4 mice/subset in 4 experiments).
Statistical differences were determined by unpaired two-tailed t-test (a,c-d), One-way ANOVA (e,h) or Two-way ANOVA (b,f) with Tukey's multiple comparisons test, and Mantel-Cox test for survival (b,f).

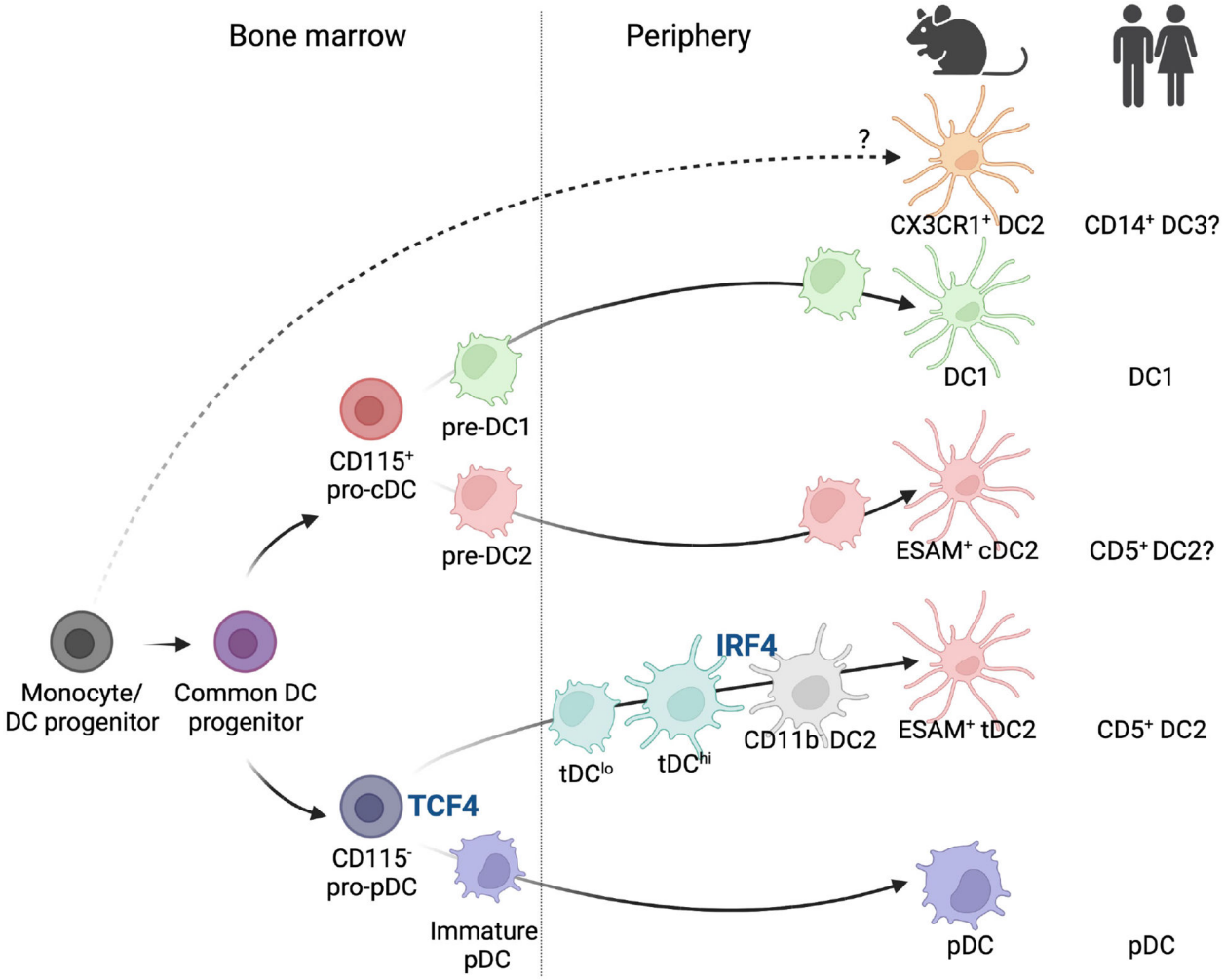

Extended Data Fig. 10. Summary of DC development at steady state.

Supplementary Material

Refer to Web version on PubMed Central for supplementary material.

ACKNOWLEDGMENTS

This work was supported by NIH grants to J.I. (AI158808 and AI163775), B.R. (AI072571, AI147501 and AI128949), and O.A.P. (CA232666). F.B.S. and R.A.H are recipient of the Dean's fellowship (Stanford), R.M-A. is supported by a fellowship from SECTEI (CDMX, Mexico), H.M.R-M. by NSF GRFP fellowship (#2019276237), N.M.A. by the Damon Runyon postdoctoral fellowship (DRG 2408-20), and A.G-B. by a KL2 Mentored Career Development Award (KL2TR003143). CyTOF was performed on the Stanford FACS Facility instrument funded by S10OD016318-01. We thank the Idoyaga and Reizis Lab members for technical support and discussions.

DATA AVAILABILITY

Mass cytometry data generated in this study are deposited in FlowRepository (FR-FCM-Z6CW, FR-FCM-Z6CN and FR-FCM-Z6CK). RNAseq data generated in this study are deposited in NCBI GEO (GSE198553 and GSE198720). NanoString data is deposited in NCBI GEO (GSE233143). All other data generated in this study are included in the source data files.

CODE AVAILABILITY

This study did not generate unique codes.

REFERENCES

1. Guilliams M. et al. Dendritic cells, monocytes and macrophages: a unified nomenclature based on ontogeny. Nat Rev Immunol 14, 571–578 (2014). [PubMed: 25033907]
2. Reizis B. Plasmacytoid Dendritic Cells: Development, Regulation, and Function. Immunity 50, 37–50 (2019). [PubMed: 30650380]
3. Alcántara-Hernández M. et al. High-Dimensional Phenotypic Mapping of Human Dendritic Cells Reveals Interindividual Variation and Tissue Specialization. Immunity 47, 1037–1050.e6 (2017). [PubMed: 29221729]
4. Leylek R. et al. Integrated Cross-Species Analysis Identifies a Conserved Transitional Dendritic Cell Population. Cell Reports 29, 3736–3750.e8 (2019). [PubMed: 31825848]
5. See P. et al. Mapping the human DC lineage through the integration of high-dimensional techniques. Science 356, eaag3009 (2017). [PubMed: 28473638]
6. Villani A-C et al. Single-cell RNA-seq reveals new types of human blood dendritic cells, monocytes, and progenitors. Science 356, eaah4573 (2017). [PubMed: 28428369]
7. Feng J. et al. Clonal lineage tracing reveals shared origin of conventional and plasmacytoid dendritic cells. Immunity 55, 405–422.e11 (2022). [PubMed: 35180378]
8. Naik SH et al. Development of plasmacytoid and conventional dendritic cell subtypes from single precursor cells derived in vitro and in vivo. Nat Immunol 8, 1217–1226 (2007). [PubMed: 17922015]
9. Onai N. et al. Identification of clonogenic common Flt3+M-CSFR+ plasmacytoid and conventional dendritic cell progenitors in mouse bone marrow. Nat Immunol 8, 1207–1216 (2007). [PubMed: 17922016]
10. Grajales-Reyes GE et al. Batf3 maintains autoactivation of Irf8 for commitment of a CD8α+ conventional DC clonogenic progenitor. Nat Immunol 16, 708–717 (2015). [PubMed: 26054719]

11. Schlitzer A. et al. Identification of cDC1- and cDC2-committed DC progenitors reveals early lineage priming at the common DC progenitor stage in the bone marrow. Nat Immunol 16, 718–728 (2015). [PubMed: 26054720]
12. Nutt SL & Chopin M Transcriptional Networks Driving Dendritic Cell Differentiation and Function. Immunity 52, 942–956 (2020). [PubMed: 32553180]
13. Bosteels C & Scott CL Transcriptional regulation of DC fate specification. Mol Immunol 121, 38–46 (2020). [PubMed: 32151907]
14. Anderson DA, Dutertre C-A, Ginhoux F & Murphy KM Genetic models of human and mouse dendritic cell development and function. Nat Rev Immunol 21, 101–115 (2021). [PubMed: 32908299]
15. Schlitzer A. et al. IRF4 transcription factor-dependent CD11b+ dendritic cells in human and mouse control mucosal IL-17 cytokine responses. Immunity 38, 970–983 (2013). [PubMed: 23706669]
16. Brown CC et al. Transcriptional Basis of Mouse and Human Dendritic Cell Heterogeneity. Cell 179, 846–863.e24 (2019). [PubMed: 31668803]
17. Lewis KL et al. Notch2 Receptor Signaling Controls Functional Differentiation of Dendritic Cells in the Spleen and Intestine. Immunity 35, 780–791 (2011). [PubMed: 22018469]
18. Satpathy AT et al. Notch2-dependent classical dendritic cells orchestrate intestinal immunity to attaching-and-effacing bacterial pathogens. Nat Immunol 14, 937–948 (2013). [PubMed: 23913046]
19. Tussiwand R. et al. Klf4 expression in conventional dendritic cells is required for T helper 2 cell responses. Immunity 42, 916–928 (2015). [PubMed: 25992862]
20. Bourdely P. et al. Transcriptional and Functional Analysis of CD1c+ Human Dendritic Cells Identifies a CD163+ Subset Priming CD8+CD103+ T Cells. Immunity 53, 335–352.e8 (2020). [PubMed: 32610077]
21. Cytlak U. et al. Differential IRF8 Transcription Factor Requirement Defines Two Pathways of Dendritic Cell Development in Humans. Immunity 53, 353–370.e8 (2020). [PubMed: 32735845]
22. Dutertre C-A et al. Single-Cell Analysis of Human Mononuclear Phagocytes Reveals Subset-Defining Markers and Identifies Circulating Inflammatory Dendritic Cells. Immunity 51, 573–589.e8 (2019). [PubMed: 31474513]
23. Bar-On L. et al. CX3CR1+ CD8α+ dendritic cells are a steady-state population related to plasmacytoid dendritic cells. Proc National Acad Sci 107, 14745–14750 (2010).
24. Valente M. et al. Novel mouse models based on intersectional genetics to identify and characterize plasmacytoid dendritic cells. Nat Immunol 24, 714–728 (2023). [PubMed: 36928414]
25. Rodrigues PF et al. Distinct progenitor lineages contribute to the heterogeneity of plasmacytoid dendritic cells. Nat Immunol 19, 711–722 (2018). [PubMed: 29925996]
26. Rodrigues PF et al. pDC-like cells are pre-DC2 and require KLF4 to control homeostatic CD4 T cells. Sci Immunol 8, eadd4132 (2023). [PubMed: 36827419]
27. Cervantes-Barragán L. et al. Control of coronavirus infection through plasmacytoid dendritic-cell-derived type I interferon. Blood 109, 1131–1137 (2007). [PubMed: 16985170]
28. Cervantes-Barragan L. et al. Plasmacytoid dendritic cells control T-cell response to chronic viral infection. Proc National Acad Sci 109, 3012–3017 (2012).
29. Leylek R. et al. Chromatin Landscape Underpinning Human Dendritic Cell Heterogeneity. Cell Reports 32, 108180 (2020). [PubMed: 32966789]
30. Dress RJ et al. Plasmacytoid dendritic cells develop from Ly6D+ lymphoid progenitors distinct from the myeloid lineage. Nat Immunol 20, 852–864 (2019). [PubMed: 31213723]
31. Siegemund S, Shepherd J, Xiao C & Sauer K hCD2-iCre and Vav-iCre mediated gene recombination patterns in murine hematopoietic cells. PloS one 10, e0124661 (2015). [PubMed: 25884630]
32. Kaitani A. et al. Leukocyte mono-immunoglobulin-like receptor 8 (LMIR8)/CLM-6 is an FcRγ-coupled receptor selectively expressed in mouse tissue plasmacytoid dendritic cells. Scientific Reports 8, 8259–13 (2018). [PubMed: 29844322]
33. Abbas A. et al. The activation trajectory of plasmacytoid dendritic cells in vivo during a viral infection. Nat Immunol 21, 983–997 (2020). [PubMed: 32690951]

34. Naik SH et al. Cutting Edge: Generation of Splenic CD8+ and CD8− Dendritic Cell Equivalents in Fms-Like Tyrosine Kinase 3 Ligand Bone Marrow Cultures. J Immunol 174, 6592–6597 (2005). [PubMed: 15905497]
35. Kirkling ME et al. Notch Signaling Facilitates In Vitro Generation of Cross-Presenting Classical Dendritic Cells. Cell Reports 23, 3658–3672.e6 (2018). [PubMed: 29925006]
36. Cabeza-Cabrerizo M. et al. Recruitment of dendritic cell progenitors to foci of influenza A virus infection sustains immunity. Sci Immunol 6, eabi9331–eabi9331 (2021). [PubMed: 34739343]
37. Liu K. et al. In vivo analysis of dendritic cell development and homeostasis. Science 324, 392–397 (2009). [PubMed: 19286519]
38. Manh TV, Alexandre Y, Baranek T, Crozat K & Dalod M Plasmacytoid, conventional, and monocyte-derived dendritic cells undergo a profound and convergent genetic reprogramming during their maturation. Eur. J. Immunol 43, 1706–1715 (2013). [PubMed: 23553052]
39. Bawazeer AO et al. Interleukin-1β exacerbates disease and is a potential therapeutic target to reduce pulmonary inflammation during severe influenza A virus infection. Immunol Cell Biol 99, 737–748 (2021). [PubMed: 33834544]
40. Grabherr S. et al. An Innate Checkpoint Determines Immune Dysregulation and Immunopathology during Pulmonary Murine Coronavirus Infection. J Immunol 210, 774–785 (2023). [PubMed: 36715496]
41. Yun TJ et al. Human plasmacytoid dendritic cells mount a distinct antiviral response to virus-infected cells. Sci Immunol 6, (2021).
42. Meredith MM et al. Zinc finger transcription factor zDC is a negative regulator required to prevent activation of classical dendritic cells in the steady state. J Exp Med 209, 1583–1593 (2012). [PubMed: 22851594]
43. Salvermoser J. et al. Clec9a-Mediated Ablation of Conventional Dendritic Cells Suggests a Lymphoid Path to Generating Dendritic Cells In Vivo. Front Immunol 9, 699 (2018). [PubMed: 29713321]
44. Lutz K. et al. Ly6D+Siglec-H+ precursors contribute to conventional dendritic cells via a Zbtb46+Ly6D+ intermediary stage. Nat Commun 13, 3456 (2022). [PubMed: 35705536]
45. Papaioannou NE et al. Environmental signals rather than layered ontogeny imprint the function of type 2 conventional dendritic cells in young and adult mice. Nat Commun 12, 464 (2021). [PubMed: 33469015]
46. Schulte-Schrepping J. et al. Severe COVID-19 Is Marked by a Dysregulated Myeloid Cell Compartment. Cell 182, 1419–1440.e23 (2020). [PubMed: 32810438]
47. Mann ER et al. Longitudinal immune profiling reveals key myeloid signatures associated with COVID-19. Sci Immunol 5, eabd6197 (2020). [PubMed: 32943497]
48. Severa M. et al. Differential plasmacytoid dendritic cell phenotype and type I Interferon response in asymptomatic and severe COVID-19 infection. Plos Pathog 17, e1009878 (2021). [PubMed: 34473805]
49. Hadjadj J. et al. Impaired type I interferon activity and inflammatory responses in severe COVID-19 patients. Science 369, 718–724 (2020). [PubMed: 32661059]
50. Geng J, Wang F, Huang Z, Chen X & Wang Y Perspectives on anti-IL-1 inhibitors as potential therapeutic interventions for severe COVID-19. Cytokine 143, 155544 (2021). [PubMed: 33926774]

METHODS-ONLY REFERENCES

51. Persson EK et al. IRF4 Transcription-Factor-Dependent CD103+CD11b+ Dendritic Cells Drive Mucosal T Helper 17 Cell Differentiation. Immunity 38, 958–969 (2013). [PubMed: 23664832]
52. Alcántara-Hernández M & Idoyaga J Mass cytometry profiling of human dendritic cells in blood and tissues. Nat Protoc 16, 4855–4877 (2021). [PubMed: 34480131]
53. Diggins KE, Greenplate AR, Leelatian N, Wogsland CE & Irish JM Characterizing cell subsets using marker enrichment modeling. Nat Methods 14, 275–278 (2017). [PubMed: 28135256]
54. Spitzer MH et al. An interactive reference framework for modeling a dynamic immune system. Science 349, 1259425 (2015). [PubMed: 26160952]

55. Love MI, Huber W & Anders S Moderated estimation of fold change and dispersion for RNA-seq data with DESeq2. Genome Biol 15, 550 (2014). [PubMed: 25516281]
56. Stephens M. False discovery rates: a new deal. Biostatistics 18, kxw041 (2016).
57. Stuart T. et al. Comprehensive Integration of Single-Cell Data. Cell 177, 1888–1902.e21 (2019). [PubMed: 31178118]
58. Tang KH et al. Combined Inhibition of SHP2 and CXCR1/2 Promotes Antitumor T-cell Response in NSCLC. Cancer Discov 12, 47–61 (2021). [PubMed: 34353854]
59. Subramanian A. et al. Gene set enrichment analysis: A knowledge-based approach for interpreting genome-wide expression profiles. Proc National Acad Sci 102, 15545–15550 (2005).
60. Mootha VK et al. PGC-1alpha-responsive genes involved in oxidative phosphorylation are coordinately downregulated in human diabetes. Nature genetics 34, 267–273 (2003). [PubMed: 12808457]
61. Newman AM et al. Determining cell type abundance and expression from bulk tissues with digital cytometry. Nat Biotechnol 37, 773–782 (2019). [PubMed: 31061481]
62. Street K. et al. Slingshot: cell lineage and pseudotime inference for single-cell transcriptomics. BMC genomics 19, 477–16 (2018). [PubMed: 29914354]
63. Manno GL et al. RNA velocity of single cells. Nature 560, 494–498 (2018). [PubMed: 30089906]
64. Bergen V, Lange M, Peidli S, Wolf FA & Theis FJ Generalizing RNA velocity to transient cell states through dynamical modeling. Nat Biotechnol 38, 1408–1414 (2020). [PubMed: 32747759]

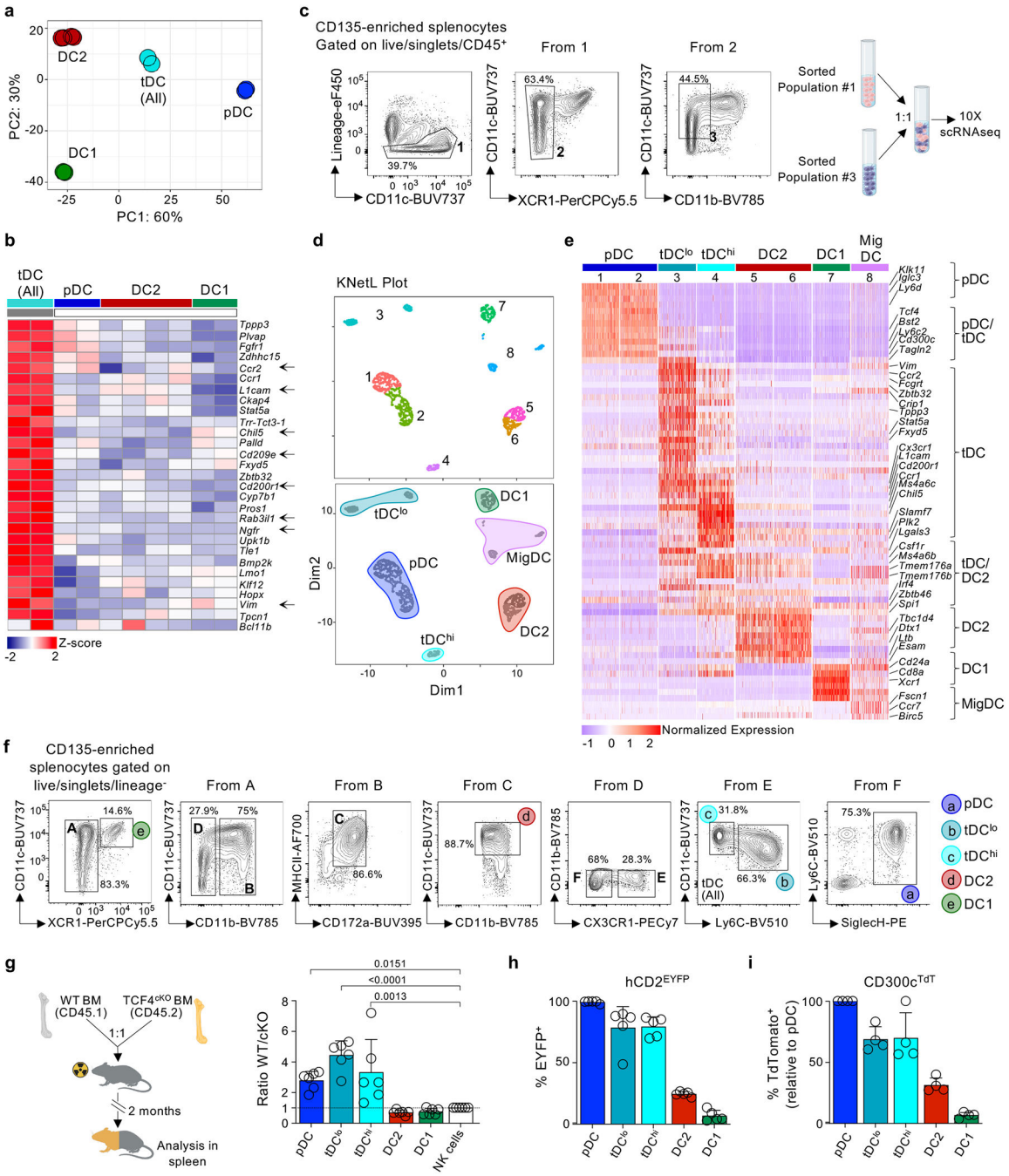

FIGURE 1. tDC are a distinct DC population developmentally related to pDC.

a. Spleen DC subsets were sorted from *hCD2*$^{Cre+/-}$ *Rosa26*$^{EYFP+/-}$ (hCD2^{EYFP}) mice as shown in Fig.1f and Extended Data Fig.1a (our rationale for using hCD2^{EYFP} mice is explained in Fig.4), and prepared for bulk RNAseq analysis. PCA plot of the top 500 most variable DEG in each DC subset (differences between EYFP^{+} and EYFP^{-} DC2 are analyzed in Fig.4).

b. Heatmap of selected genes from (a). Shown is Z-score of normalized expression.

c. Splenocytes of WT mice were enriched in $CD135^+$ cells and stained for cell sorting. Populations #1 and #3 were purified, mixed 1:1 and processed for droplet-based genomics. Excluded lineage contains $CD3^+/CD19^+/NK1.1^+/Ly6G^+$ cells.

d. KNetL plot of scRNAseq data. After filtering and removing a small fraction of monocytes, 2,075 cells were analyzed using the KNetL pipeline. Shown are KNetL clusters (top) and annotations based on subset-specific scores using CIBERSORTx (bottom) (Extended Data Fig.1f).

e. Heatmap of selected genes differentially expressed in (d) clusters. Gene expression after normalization and imputation is shown.

f. Gating strategy used for the analysis of spleen DC subsets. CD135-enriched splenocytes were stained and analyzed by flow cytometry. Excluded lineage contains $CD3^+/CD19^+/NK1.1^+/Ly6G^+$ cells.

g. Left shows schematic of BMC generated by transplanting 50% WT (CD45.1) and 50% $TCF4^{cKO}$ (CD45.2) BM into lethally irradiated CD45.1 WT mice. Right shows bar graphs (mean + SD) of the contribution of donor cells to splenic DC populations (gated as in Fig.1f) in BMC, normalized to NK cells (n=6 mice in 2 experiments). Statistics were determined by one-way ANOVA with Dunnett's multiple comparison test.

h. Bar graph (mean + SD) showing the percentage of $EYFP^+$ splenic DC (gated as in Fig.1f) in $hCD2^{EYFP}$ mice (n=5 mice in 4 experiments).

i. Bar graph (mean + SD) showing the percentage of $TdTomato^+$ splenic DC (gated as in Fig.1f) in $CD300c^{TdT}$ mice. Percentage relative to pDC is shown (n=4 mice in 3 experiments; see also Extended Data Fig.2c).

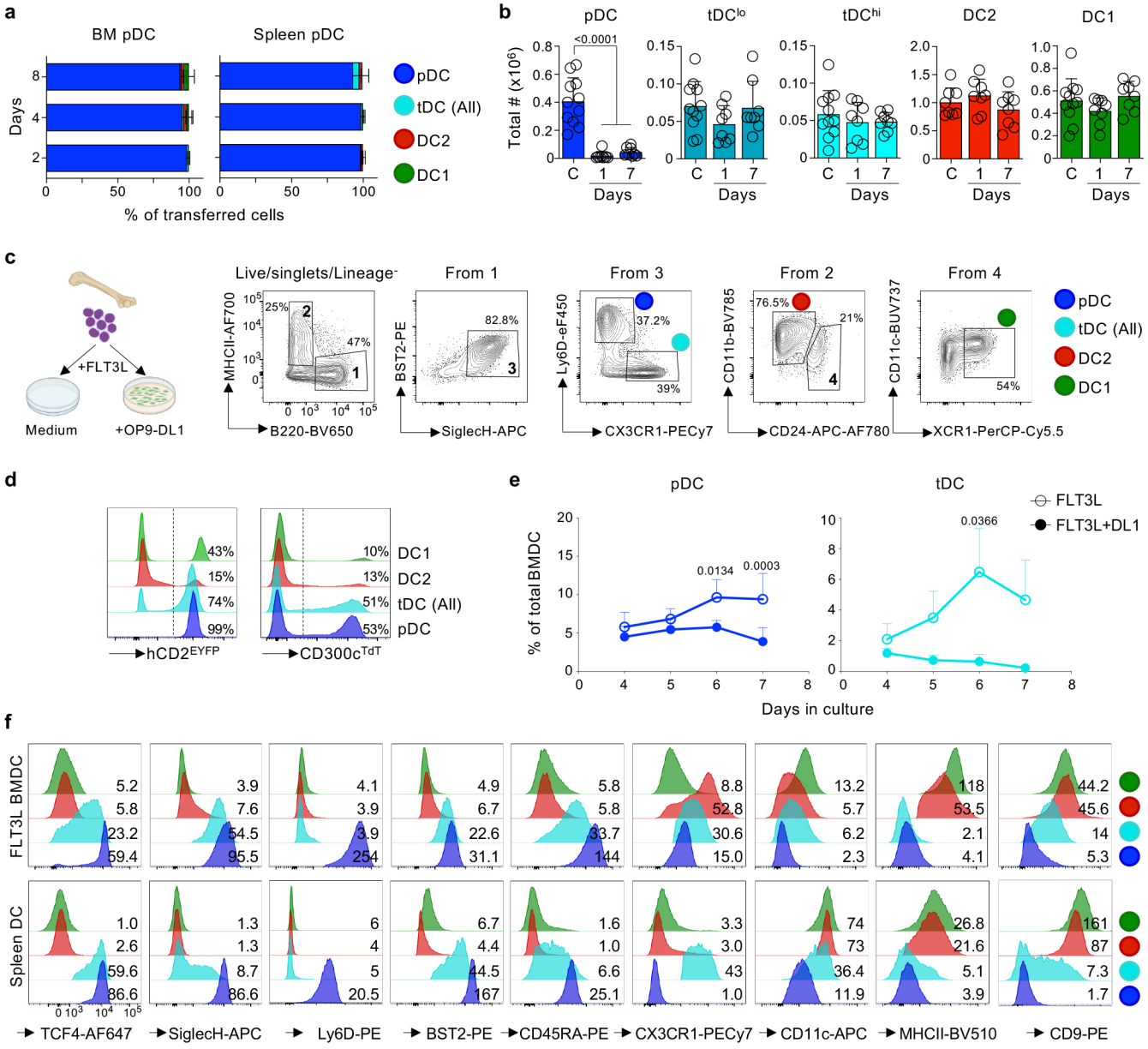

FIGURE 2. tDC originate from BM progenitors.

a. Percentage (mean + SD) of each DC subset recovered after the adoptive transfer of 30,000 BM or splenic CX3CR1^{EGFP} CD45.1 pDC into CD45.2 WT non-irradiated congenic mice. Transferred cells were analyzed in the spleen of recipient mice after 2-8 days. BM: n=4 at 2- and 4-days, and n=3 at 8-days. Spleen: n=3 at 2- and 4-days, and n=2 at 8-days. N represents mice and experiments.

b. Bar graphs (mean + SD) of the total number of each splenic DC subset (gated a in Fig.1f) in littermate controls (C; n=11 *BDCA2*-DTR$^{-/-}$ mice) or *BDCA2*-DTR$^{+/-}$ mice inoculated with DT and analyzed 1 day later (n=8 mice), or inoculated with DT every second day and analyzed at day 7 (n=8 mice). Data pooled from 5 exp. Statistical differences were determined by one-way ANOVA with Tukey's multiple comparison test.

c. Left shows schematic of BM cells cultured with FLT3L +/− OP9-DL1 cells. Right shows the gating strategy to detect DC subsets at 6-days of BM culture, analyzed by flow cytometry (excluded lineage contains $CD3^+/CD19^+/F4/80^+$ cells). One representative of 5 experiments.

d. Histograms of $hCD2^{EYFP}$ (left) or $CD300c^{TdT}$ (right) expression in BM-derived DC as defined in (c), analyzed at 6-days. One representative of 3 experiment.

e. pDC and tDC percentage (mean + SD) in BM cultures from (c), gated on total live and single cells. N=5 samples/time point, except n=6 samples for FLT3L+DL1 at 4-days. Data pooled from ≥ 5 experiments. Statistical differences were determined by Two-way ANOVA with Sidak multiple comparisons test.

f. Histograms of protein expression of DC markers in BM-derived DC as defined in (c) or splenic DC as defined in Fig.1f. Number indicates gMFI x 10^2. One representative of 3 experiments.

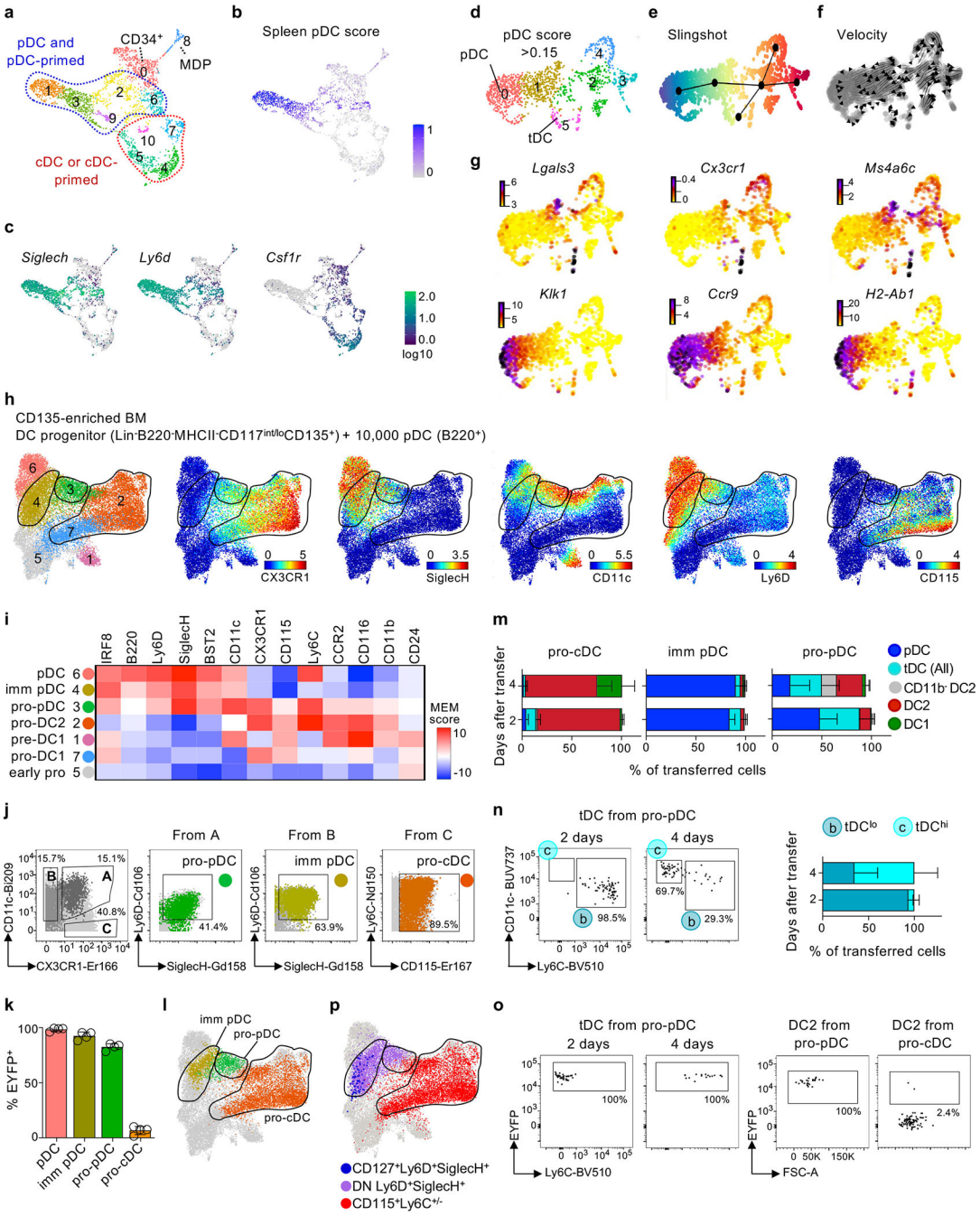

FIGURE 3. tDC originate from pro-pDC.

a. CD135-enriched BM cells were sorted as live/singlets/CD45$^+$/Lineage$^-$ (CD3$^-$/CD19$^-$/CD335$^-$/Ly6G$^-$) cells and prepared for scRNAseq using droplet-based genomics. After filtering for low quality cells, 2831 cells were clustered using Seurat and represented in a UMAP.

b. Splenic pDC-signature in BM progenitors. A signature matrix was generated using RNAseq data of splenic DC and CIBERSORTx. Labeled are cells with a positive gene enrichment score.

c. UMAP showing the expression of the indicated genes.
d. UMAP of "pDC^{high}" cells in the BM. Cells from (b) with a pDC-specific gene enrichment score of >0.15 were selected and re-clustered using Seurat.
e. Inference of differentiation trajectory of the clusters defined in (d) using Slingshot.
f. Inference of differentiation trajectory of the clusters defined in (d) using RNA velocity. Velocity vector is indicated as streamlines.
g. Velocity illustrating the expression of selected pDC- and tDC- specific genes.
h. Unbiased X-shift clustering of BM progenitors analyzed by CyTOF and represented by UMAP. CD135-enriched BM cells were gated as Lineage$^-$ (CD3$^-$/CD19$^-$/CD335$^-$/Ly6G$^-$) B220$^-$/MHCII$^-$/CD117$^{int\text{-}lo}$/CD135$^+$, and concatenated with 10,000 B220$^+$ pDC (left). UMAP was plotted based on the expression of all markers excluding lineage, and colored based on the expression of the indicated proteins (right).
i. Heatmap depicting marker enrichment modeling (MEM) scores in clusters identified in (h). imm pDC: immature pDC; early pro: early progenitors.
j. CD135-enriched BM cells were gated as Lineage$^-$ (CD3$^-$/CD19$^-$/ CD335$^-$/ Ly6G$^-$) B220$^-$/MHCII$^-$/ CD117$^{int\text{-}lo}$/CD135$^+$ as in (h). Graphs show bi-axial gating strategy to identify immature pDC (cluster 4; CD11c$^+$CX3CR1$^-$Ly6D$^+$SiglecH$^+$), pro-pDC (cluster 3; CD11c$^+$CX3CR1$^+$Ly6D$^+$SiglecH$^+$) and pro-cDC (clusters 2 and 7; CD11c$^-$CX3XR1$^+$CD115$^+$ Ly6C$^{+/-}$).
k. Bar graph (mean + SD) showing the percentage of BM pDC, imm pDC, pro-pDC and pro-cDC labeled with EYFP in hCD2^{EYFP} mice. N=4 mice and 4 independent experiments.
l. Clusters gated as in (j) were overlaid on the CyTOF UMAP of (h).
m. 15,000-30,000 pro-cDC, imm pDC or pro-pDC sorted from BM of CX3CR1^{EGFP} CD45.1 mice using the strategy described in (j) were adoptively transferred into non-irradiated WT CD45.2 congenic mice. The spleen of recipient mice was analyzed 2-4-days later to evaluate the outcome of transferred cells. Shown is the percentage (mean + SD) of each DC subset recovered in the spleen of recipient mice. Pro-cDC: n=3 at 2-days and n=5 at 4-days. Imm pDC: n=3 at 2- and 4-days. Pro-pDC: n=3 at 2-days and n=5 at 4-days. N represents number of mice and independent experiments.
n. As in (m), but splenic tDC recovered following the adoptive transfer of pro-pDC were further divided into tDC^{lo} and tDC^{hi}. A representative gating strategy (left) and percentage (mean + SD) of each tDC population (right) are shown. N=3 at 2-days and n=5 at 4-days. N represents number of mice and independent experiments.
o. As in (m), but progenitors were sorted from hCD2^{EYFP} mice and adoptively transferred into congenic non-irradiated recipients. The spleen of recipient mice was analyzed for the presence of transferred cells at 4-days, which were gated as described in Fig.1f and further analyzed for EYFP expression. Shown are tDC recovered after the adoptive transfer of pro-pDC (left), DC2 recovered after the adoptive transfer of pro-pDC (middle), and DC2 recovered after the adoptive transfer of pro-cDC (right). One representative of 3 exp.
p. Clusters gated as in Extended Data Fig.4a were overlaid on the CyTOF UMAP of (h).

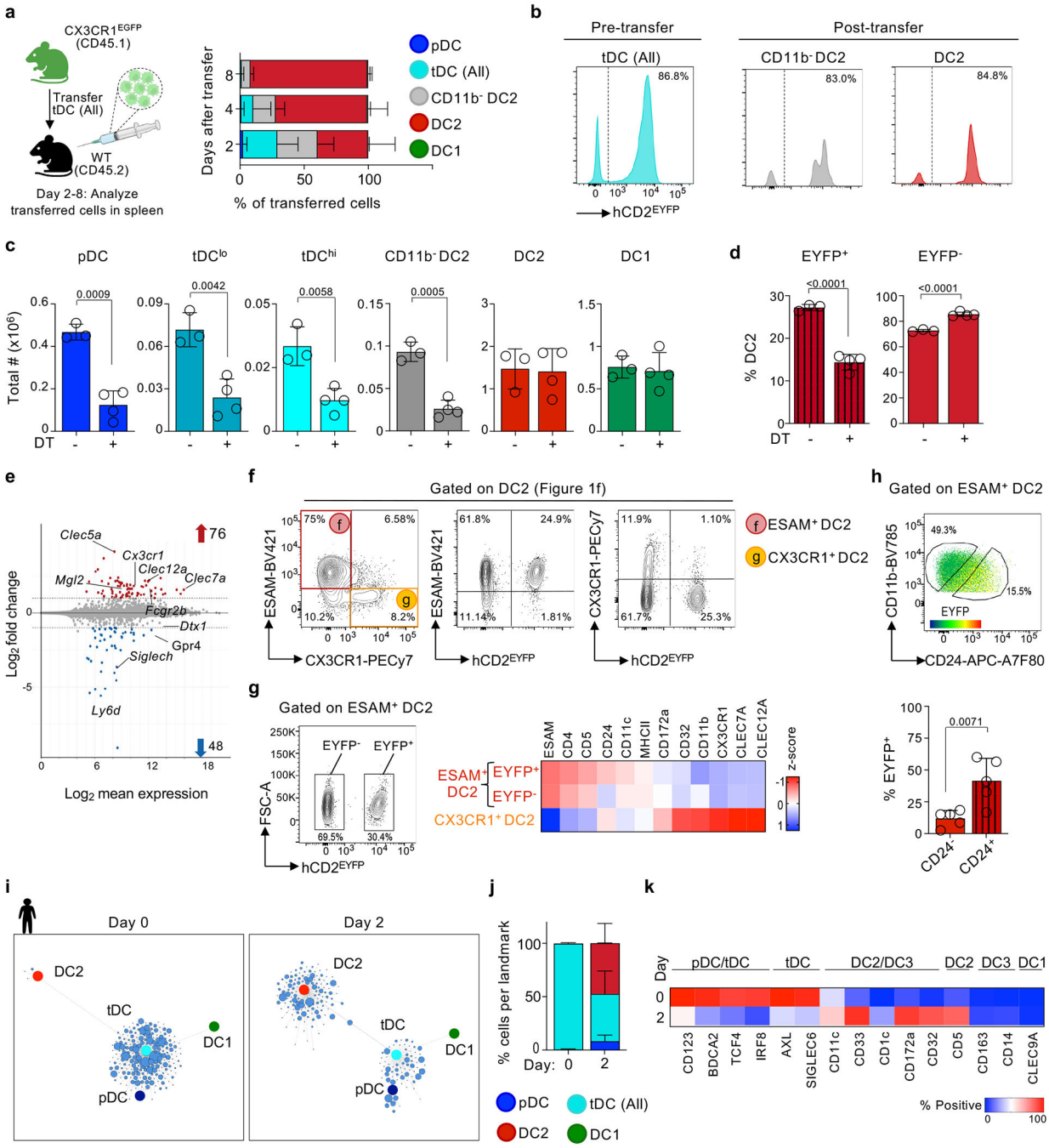

FIGURE 4. tDC convert into mouse ESAM^{+} DC2 and human CD5^{+} DC2.

a. Schematic of adoptive transfer (left). 30,000 splenic tDC (All) sorted from CX3CR1^{EGFP} CD45.1 mice using Fig.1f gating strategy, and adoptively transferred into WT CD45.2 non-irradiated congenic mice. The percentage (mean + SD) of each DC subset recovered in the spleen of recipient mice is shown 2-8 days after transfer. N=5 at 2-days, n=6 at 4-days, and n=4 at 8-days. N represents number of mice and independent experiments.

b. As in (a), but tDC were sorted from hCD2^{EYFP} mice. Histograms of hCD2^{EYFP} expression in sorted tDC pre-transfer (left), and CD11b^{-} and CD11b^{+} DC2 recovered in the spleen of recipient mice at 8-days. One representative of 2 experiments.

c. Bar graphs (mean + SD) of the total number of splenic DC subsets (gated a Fig.1f) in hCD2^{EYFP} CX3CR1^{DTR} mice inoculated (n=4 mice) or not (n=3 mice) with DT every second day and analyzed at day 7. Statistics were determined by unpaired two-tailed t-test. Data pooled from 2 experiments.

d. As in (c), but DC2 gated as in Fig.1f were further divided in EYFP^{+} and EYFP^{-} cells, and their frequencies were plotted.

e. Splenic EYFP^{+} and EYFP^{-} DC2 were sorted from hCD2^{EYFP} mice and prepared for bulk-RNAseq analysis (Extended Data Fig.1a). MA plot comparing differences between EYFP^{+} and EYFP^{-} DC2. Genes with 2-fold Log_2 change are colored in red (up) or blue (down).

f. Splenic DC2 from hCD2^{EYFP} mice were gated as in Fig.1f and further analyzed to delineate ESAM^{+} and CX3CR1^{+} subpopulations (left). EYFP expression in ESAM^{+} and CX3CR1^{+} DC2 (right). One representative of 8 experiments.

g. DC2 from the spleen of hCD2^{EYFP} mice were gated on CX3CR1^{+}, ESAM^{+} EYFP^{+} and EYFP^{-} as shown in (f)(left). Each DC2 subpopulation was analyzed for their relative expression of surface markers. Heatmap shows the Z-scored gMFI (right). Z-score values was determined from n ≥ 2 mice. Data pooled from 8 independent experiments.

h. Dot plot of ESAM^{+} DC2 gated as in (f) was colored base on EYFP expression (top). Bar graph (mean + SD) showing the percentage of EYFP^{+} in ESAM^{+} CD24^{-} and ESAM^{+} CD24^{+} (bottom)(n=5 mice in 4 experiments). Statistics were determined by unpaired two-tailed t-test.

i. Freshly isolated tDC were sorted from human blood and stimulated with CD40L for 2-days. Cells were analyzed by CyTOF and Scaffold at time 0 and 2-days post-stimulation (n=3 samples in 3 independent experiments).

j. As in (i), but bar graph shows the frequency (mean + SD) of tDC mapped to each scaffold landmark node at day 0 and 2 post-stimulation. N=2 at 0 days and n=3 at 2-days. N represents number of samples and independent experiments.

k. Heatmap of the expression of the indicated markers in freshly isolated (day 0) and stimulated (day 2) human tDC analyzed by CyTOF and flow cytometry. The frequency of positive cells for each marker is shown (≥ 2 donors/per marker in ≥ 2 experiments).

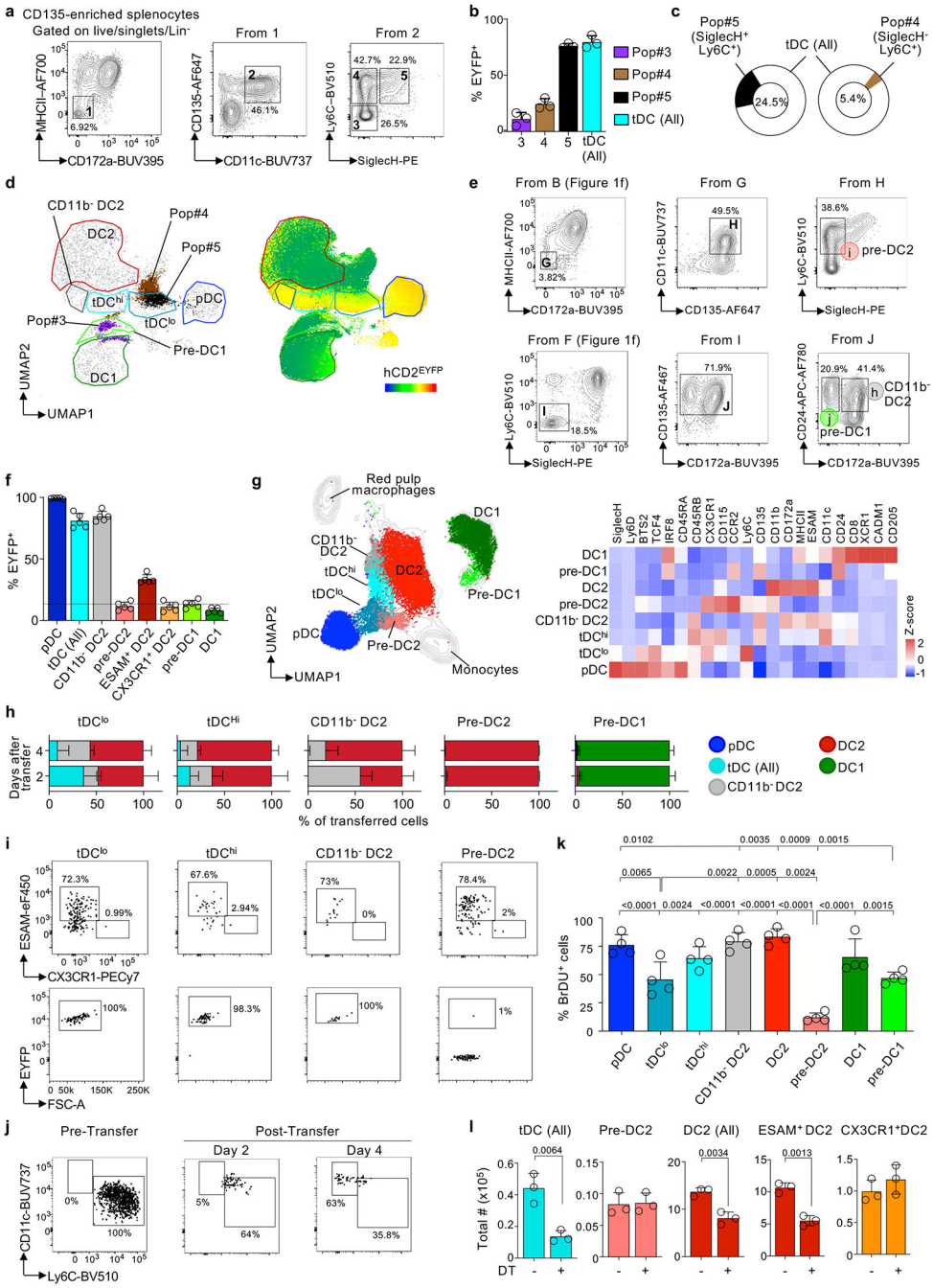

FIGURE 5. tDC are distinct from pre-cDC.

a. CD135-enriched splenic cells were stained for flow cytometry to identify pre-cDC. Lineage includes $CD3^+/CD19^+/NK1.1^+/Ly6G^+$ cells. One representative of 3 experiments.

b. Populations gated as in (a) were analyzed for their percentage of $EYFP^+$ (mean + SD) in $hCD2^{EYFP}$ mice (n=3 mice in 3 experiments). tDC were gated as in Fig.1f.

c. Frequency of pop#4 and pop#5 within the tDC gate is shown as the mean of n=3 mice in 3 experiments.

d. CD135-enriched splenocytes from hCD2^{EYFP} mice were labeled for flow cytometry, gated as live/singlets/CD3^{-}/CD19^{-}/NK1.1^{-}/Ly6G^{-} cells and analyzed by UMAP. DC subset assignment (left) was done by gating cells as in Fig.1f. UMAP was labeled for EYFP (right). One representative of 3 experiments.

e. CD135-enriched splenocytes gated as in Fig.1f were further analyzed for the identification of CD11b^{-} DC2, pre-DC2 and pre-DC1. One representative of 5 experiments.

f. Splenocytes from hCD2^{EYFP} mice gated as in Fig.1f and Fig.5e were analyzed for the frequency (mean + SD) of EYFP^{+} cells. N=5 mice in 5 experiments.

g. CD135-enriched splenocytes were stained and analyzed by CyTOF. CD3^{-}/CD19^{-}/NK1.1^{-}/Ly6G^{-} cells were gated as in Fig.1f and Fig.5e, and overlaid into the UMAP of all cells (left)(n=3 mice in 1 exp.). Heatmap of the Z-scored expression of each marker analyzed by CyTOF or flow cytometry (right)(n=3 mice/surface marker).

h. Percentage (mean + SD) of each DC subset recovered after the adoptive transfer of 10,000-30,000 CX3CR1^{EGFP} CD45.1 cell populations (gated as described in Fig.1f and Fig.5e). Transferred cells were analyzed in the spleen of recipient mice after 2 or 4 days. tDC^{lo} and tDC^{hi}: n=3 at 2-days and n=5 at 4-days. CD11b^{-}DC2: n=3 at 2-days and n=4 at 4-days. Pre-DC2: n=3 at 2- and 4-days. Pre-DC1, n=2 at 2-days and n=4 at 4-days. N represents number of mice and independent experiments.

i. As in (h), but cells were sorted from hCD2^{EYFP} mice and adoptively transferred into congenic non-irradiated recipients. The spleen of recipient mice was analyzed for the expression of ESAM and CX3CR1 (top panels) or EYFP (bottom panels) at 4-days post-transfer. One representative of 3 experiment.

j. As in (h), but splenic cells recovered following the adoptive transfer of tDC^{lo} were analyzed as tDC^{lo} and tDC^{hi}. One representative of 3 experiments.

k. WT mice were pulsed with BrDU for 14 days. 6-8-days post-BrDU removal, DC subsets gated as in Fig.1f and Fig.5e were analyzed for their BrDU content by flow cytometry. The frequency of BrDU^{+} cells (mean + SD) is shown. N=4 mice in 2 experiments. Statistical differences were determined by one-way ANOVA with Tukey's multiple comparison test.

l. Bar graphs (mean + SD) showing the total number of splenic DC (gated a Fig.1f and Fig.5e) in hCD2^{EYFP} CX3CR1^{DTR} mice inoculated or not with DT every second day, and analyzed at day 10 (n=3 mice in two experiments). See also Extended Data Fig.6d-e. Statistical differences were determined by unpaired two-tailed t-test.

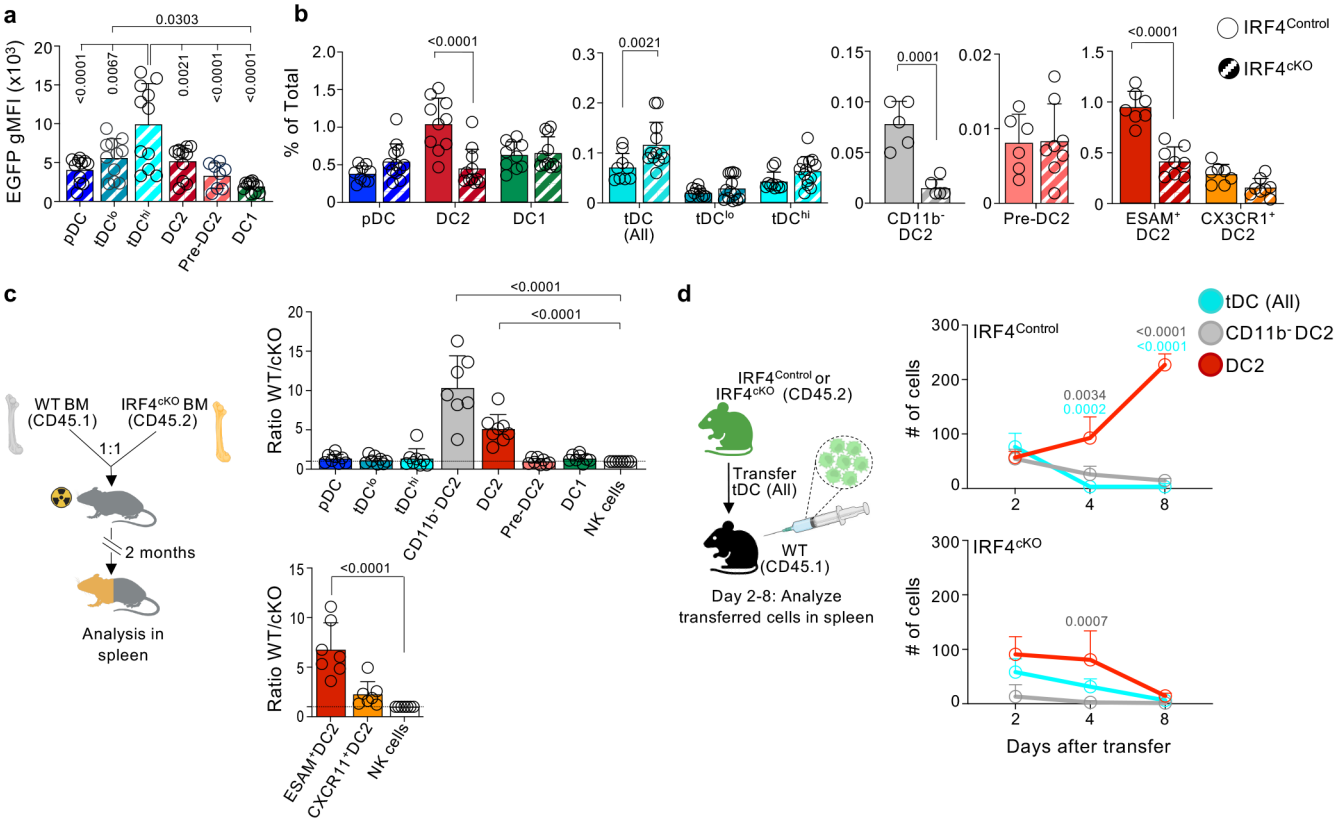

FIGURE 6. IRF4 is required for tDC transition to CD11b⁻ DC2.

a. Bar graphs (mean + SD) showing EGFP expression in splenic DC from IRF4^{cKO}, gated as described in Fig.1f and Fig.5e. N=11 mice/subset, except n=8 mice for pre-DC2, in ≥ 4 experiments. Statistical differences were determined by one-way ANOVA followed by Tukey multiple comparison test.

b. Bar graphs (mean + SD) show the frequency of DC in IRF4^{control} mice and IRF4^{cKO} mice analyzed for the proportion of each splenic DC population, gated as in Fig.1f and Fig.5e. pDC, DC2 and DC1: n=9 (IRF4^{control}) and n=11 (IRF4^{cKO}). tDC (All), tDC^{lo} and tDC^{hi}: n=9 (IRF4^{control}) and n=11 (IRF4^{cKO}). CD11b^{-}DC2: n=5 (IRF4^{control}) and n=5 (IRF4^{cKO}). Pre-DC2: n=5 (IRF4^{control}) and n=5 (IRF4^{cKO}). ESAM^{+}DC2 and CX3CR1^{+}DC2: n=7 (IRF4^{control}) and n=8 (IRF4^{cKO}). N represents mice in ≥4 independent experiments. Statistical differences were determined by two-way ANOVA with Sidak multiple comparison test, and t-test for CD11b^{-}DC2 and pre-DC2.

c. Left shows schematic of BM chimera generated by transplanting 50% WT (CD45.1) and 50% IRF4^{cKO} (CD45.2) BM. Right shows bar graphs (mean + SD) of the contribution (ratio) of donor cells to splenic DC populations (top) or DC2 subpopulations (bottom) in mixed BMC, normalized to NK cells (n=7 mice in 2 experiments). Statistical differences were determined by one-way ANOVA with Dunnett's multiple comparison test.

d. Schematic of adoptive transfer (left). 30,000 tDC (All) were sorted from CD45.2 IRF4^{control} and IRF4^{cKO}, and transferred to CD45.1 WT. Right graphs show the total # of recovered cells (mean + SD) in the spleen 2-8-days post-transfer (n=3 mice in 3 experiments/time point). Statistical differences were determined by two-way ANOVA with

Sidak multiple comparison test. Colored p-values represent statistical difference between DC2 and tDCs (cyan), or DC2 and CD11b^{-} DC2 (gray).

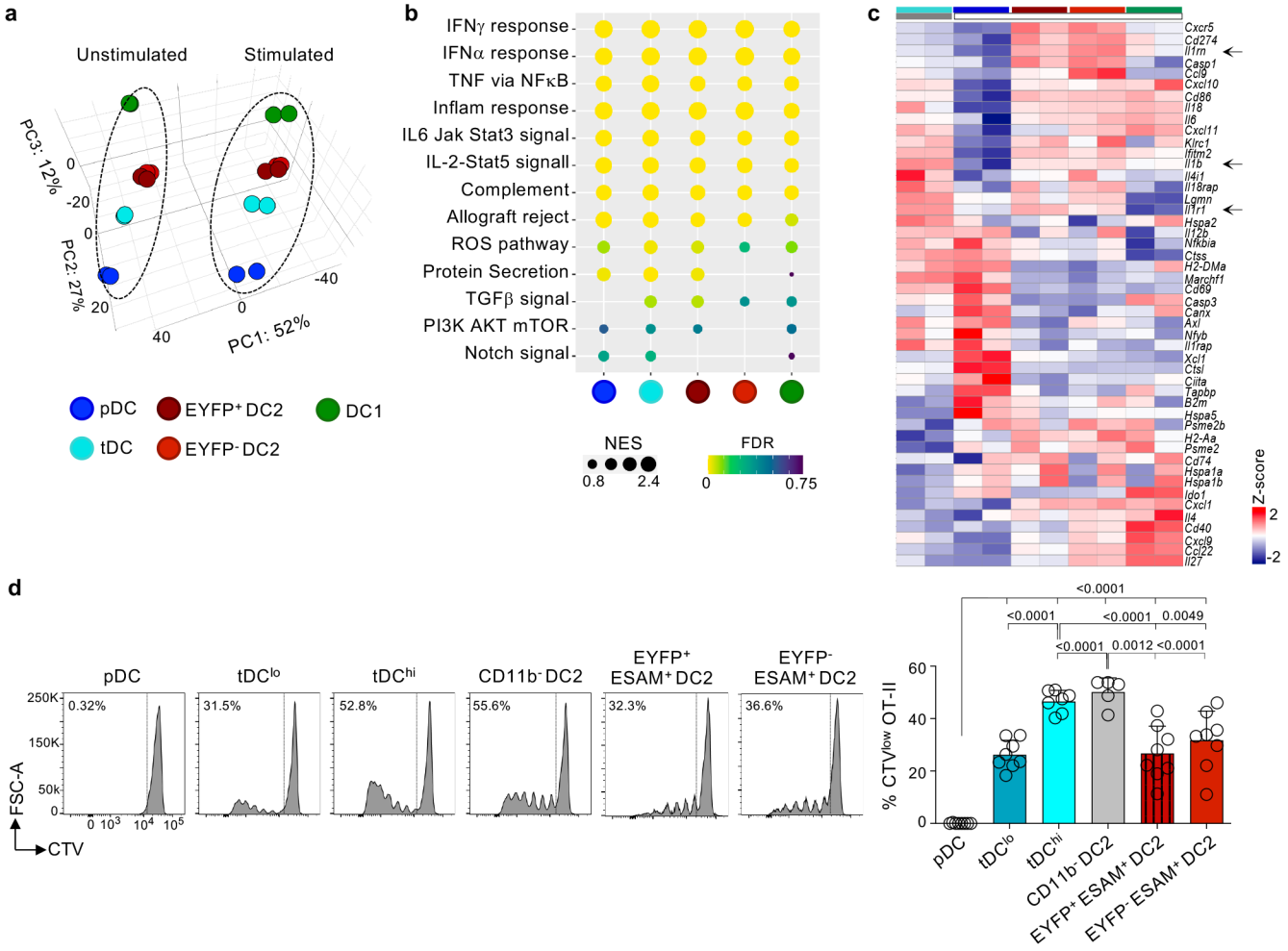

FIGURE 7. tDC respond to TLR stimulation and activate antigen-specific naïve T cells.

a. CD135-enriched splenic DC were activated or not with a cocktail of TLR agonists consistent on LPS/PolyIC/Resiquimod/CpGA (stimulated) for 3 hrs before sorting (as described in Extended Data Fig.1a), and prepared for bulk RNAseq (n=2 mice in 2 exp.). PCA plot of the top 500 most variable DEG in each unstimulated or stimulated DC subset.

b. GSEA of selected pathways using the 500 most variable DEG. Each DC subset was compared to their respective unstimulated control.

c. Heatmap of selected genes from the GSEA analysis in (b).

d. Sorted CTV-labeled naïve OT-II CD4$^+$ T cells were co-cultured with sorted splenic DC subsets (purified using the gating strategy in Fig.1f and Fig.4f) at a ratio of 5:1 (T cell:DC), in the presence of OVA protein. Four days after co-culture, cells were analyzed by flow cytometry. Left: representative flow cytometry analysis. Right: bar graphs (mean + SD) of T cell proliferation. N=5 for CD11b$^-$ DC2, n=7 for tDC^{hi}, and n=8 for all the other groups. N represents biologically independent samples in ≥ 2 experiments. Statistical differences were determined by one-way ANOVA with Tukey's multiple comparison test.

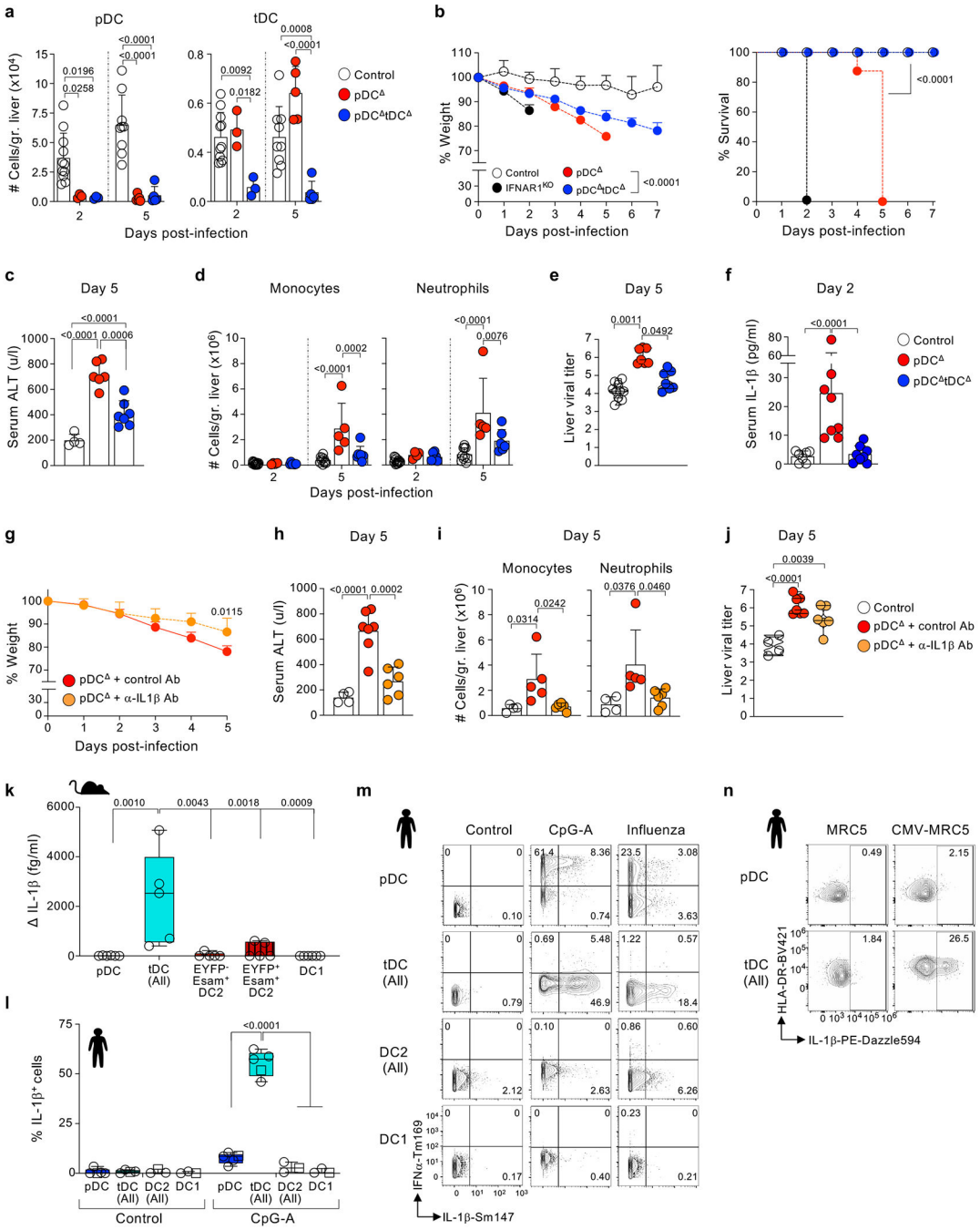

FIGURE 8. Secretion of IL-1β by tDC results in immunopathology in pDC-depleted mice.

a. Liver pDC and tDC numbers (mean + SD) at 2- and 5-days following M-CoV infection of pDC$^{\Delta}$ and pDC$^{\Delta}$tDC$^{\Delta}$ (n=3/group at 2-days and n=5/group at 5-days) vs control mice (n=11 at 2-days and n=9 at 5-days). pDC$^{\Delta}$ mice are *BDCA2*-DTR$^{+/-}$ mice inoculated with DT one day before M-CoV infection. pDC$^{\Delta}$tDC$^{\Delta}$ are hCD2^{EYFP} CX3CR1^{DTR} mice inoculated with DT every other day for 5-days before M-CoV infection. Control mice are a combination of *BDCA2*-DTR$^{+/-}$ or hCD2^{EYFP} CX3CR1^{DTR} mice inoculated with PBS, and DTR$^{-/-}$ mice

inoculated with DT (no difference in control mice was observed). N represents mice. Data pooled from ≥ 3 experiments.

b. Percent weight loss (left, mean + SD) and survival curve (right) of control (n=12), IFNAR1^{KO} (n=8), pDC$^{\Delta}$ (n=7) and pDC$^{\Delta}$tDC$^{\Delta}$ (n=8) mice. Health status was monitored twice daily, and moribund mice were euthanized. N represents mice. Data pooled from 4 experiments.

c. Serum ALT levels (mean + SD) determined 5-days post-M-CoV infection (n=4 mice for control; n=6 mice for pDC$^{\Delta}$; n=7 mice for pDC$^{\Delta}$tDC$^{\Delta}$). Data pooled from 3 independent experiments.

d. The number of liver monocytes and neutrophils (mean + SD) were evaluated by flow cytometry 2- and 5-days post-M-CoV infection as in (a). Day 2: n=14 for control, n=4 for pDC$^{\Delta}$ and n=6 mice for pDC$^{\Delta}$tDC$^{\Delta}$. Day 5: n=10 for control, n=5 mice for pDC$^{\Delta}$ and n= 6 mice for pDC$^{\Delta}$tDC$^{\Delta}$. N represents mice. Data pooled from 3 or more exp.

e. Liver viral titers (log_{10} pfu / gr. tissue) were determined 5-days post-M-CoV infection (n=10 mice for control, n=7 mice/group for pDC$^{\Delta}$ and pDC$^{\Delta}$tDC$^{\Delta}$). Violin plots show data pooled from 4 experiments.

f. Serum levels of IL-1β were determined 2-days post-M-CoV infection by Luminex (n=7 mice for control, n=8 mice/group for pDC$^{\Delta}$ and pDC$^{\Delta}$tDC$^{\Delta}$). Data pooled from 4 experiments.

g. pDC$^{\Delta}$ mice were inoculated with anti-IL-1β Ab 2-days post-M-CoV-infection, and the percent weight loss (mean + SD) was measured over time. N=5 mice for pDC$^{\Delta}$ + control Ab, and n=6 mice for pDC$^{\Delta}$ + α-IL1-β Ab. Data pooled from 3 experiments.

h. As in (g), but serum ALT levels (mean + SD) were evaluated at 5-days post-infection. N=4 mice for control, n=7 mice for pDC$^{\Delta}$ + control Ab, and n=6 mice for pDC$^{\Delta}$ + α-IL1-β Ab. Data pooled from 3 experiments.

i. As in (g), but numbers of liver monocytes and neutrophils (mean + SD) were quantified by flow cytometry at 5-days post-M-CoV infection. N=4 mice for control, n=5 mice for pDC$^{\Delta}$ + control Ab, and n=6 mice for pDC$^{\Delta}$ + α-IL1-β Ab. Data pooled from 3 independent experiments.

j. As in (g), but liver viral titers (log_{10} pfu / gr. tissue) were evaluated 5-days post-M-CoV infection. N=4 mice for control, n=7 mice for pDC$^{\Delta}$ + control Ab, and n=6 mice for pDC$^{\Delta}$ + α-IL1-β Ab. Violin plots show data pooled from 3 experiments.

k. DC subsets gated as in Fig.1f and Fig.4g were sorted and incubated with M-CoV or mock (supernatant from non-infected L929 cells) using an MOI of 1. Culture supernatant was analyzed by CBA 14-16 hrs later (n=5 samples in 3 experiments). Minimum and maximum values are indicated via whiskers, while the interquartile range and median are marked with the box.

l. Human blood enriched DCs were left unstimulated (control) or stimulated with CpG-A for 6-9 hrs, and then analyzed for intracellular IL-1β by flow cytometry (circles) or CyTOF (square). N=5 donors for tDC and pDC and n=3 donors for DC1 and DC2. Data pooled from 4 experiments. Minimum and maximum values are indicated via whiskers, while the interquartile range and median are marked with the box.

m. As in (l), but cells were stimulated with CpG-A or influenza virus, and analyzed by CyTOF in one experiment.

n. As in (l), but pDC and tDC were sorted and incubated with MRC5 fibroblast cell line alone or MRC5 infected with CMV (CMV-MRC5) for 6 hrs, and analyzed for intracellular IL-1β by flow cytometry in one experiment.

Statistical differences were determined by Two-way ANOVA with Tukey's multiple comparisons test (a-c,g), by One-way ANOVA with Tukey's multiple comparisons test (d-f,h-l) or Mantel-Cox test for survival curves (b).